8-2019

Developing Multispectral Imaging Techniques to Determine Canopy Coverage and Carbon Storage of Seagrasses in the Gulf of Mexico

Ivy Michelle Hinson
The University of Texas Rio Grande Valley

DEVELOPING MULTISPECTRAL IMAGING TECHNIQUES TO DETERMINE CANOPY COVERAGE AND CARBON STORAGE OF SEAGRASSES IN THE GULF OF MEXICO

A Thesis

by

IVY MICHELLE HINSON

Submitted to the Graduate College of
The University of Texas Rio Grande Valley
In partial fulfillment of the requirements for the degree of

MASTER of SCIENCE

August 2019

Major Subject: Ocean, Coastal, and Environmental Science

DEVELOPING MULTISPECTRAL IMAGING TECHNIQUES TO DETERMINE CANOPY COVERAGE AND CARBON STORAGE OF SEAGRASSES IN THE GULF OF MEXICO

A Thesis
by
IVY MICHELLE HINSON

COMMITTEE MEMBERS

Dr. Christopher A. Gabler
Chair of Committee

Dr. Abdullah F. Rahman
Co-chair of Committee

Dr. Hudson R. DeYoe
Committee Member

August 2019

ABSTRACT

Hinson, Ivy M. Developing multispectral imaging techniques to determine canopy coverage and carbon storage of seagrasses in the Gulf of Mexico. Master of Science (MS), August 2019, 65 pp, 8 tables, 14 figures, references, 42 titles.

Although seagrass beds provide global ecosystem services, coverage is in rapid decline, with the capacity of seagrasses to sequester carbon of special concern. Current seagrass monitoring methods are labor intensive and may not offer a complete picture of coverage. Remote sensing offers the ability to oversee landscapes but water in coastal environments presents challenges, as the commonly used near-infrared wavelength dissipates in water.

This project aimed to provide reliable methodology to assess seagrass coverage using multispectral imagery taken from an unmanned aerial vehicle and to provide evidence for the link between seagrass coverage and stored belowground carbon for common seagrasses in the Gulf of Mexico. Reflectance values from multispectral imagery produced coverage estimates that were compatible with in-water surveys and canopy coverage proved to be a reliable predictor of below-ground carbon storage, in the first 10 cm. Further research of carbon storage in gaps in seagrass cover is needed.

DEDICATION

This work is dedicated to my family and friends, all of whom always offered support, whether from across the country or across the hall.

ACKNOWLEDGEMENTS

Thank you to the many people that have contributed to this project. Funding for my work was made possible by Texas Sea Grant. My work with multispectral imagery was made possible by Digital Globe Foundation's generous contribution of Worldview II satellite imagery. A special thank you to my committee co-chairs Dr. Christopher Gabler and Dr. Abdullah Rahman, as well as committee member Dr. Hudson DeYoe for their knowledge and commitment to this project. My fieldwork would not have been possible without the help of Amy Bogolin, Gus Plamann, Andrew Corder, Douglas Faircloth, and Eberto Presas.

TABLE OF CONTENTS

LIST OF TABLES

LIST OF FIGURES

Page

CHAPTER 1

INTRODUCTION

Seagrasses are a globally distributed group of marine plants with relatively low taxonomic diversity (Orth et al., 2006). Only 60 species of seagrasses are known, yet unique adaptations have allowed these plants to thrive in water temperatures ranging from 4°C to greater than 24°C (Orth et al., 2006). Seagrasses have also evolved to grow in anoxic and often sulfide-rich sediments by enriching rhizomes and the surrounding rhizosphere with oxygen (Hemming and Durate, 2000). Seagrass rhizomes can be extensive, with 60-90% of a plant's biomass underground (Fourqurean et al., 2012). Seagrass beds can include algae, seaweed, and stray corals and often have naturally occurring bare patches and varying levels of plant density (Ruiz-Reynés, 2017).

Seagrass in the Western Gulf of Mexico

The Laguna Madre is a large, productive, hypersaline bay in the western Gulf of Mexico that spans from Corpus Christi, Texas, south to Port Isabel, Texas, near the U.S.-Mexico border, totaling a surface area of 1,658 km^2. The bay's productivity is due, in part, to the presence of seagrass under a relatively shallow 75-cm average water depth (Quammen and Onuf, 1993). With 80% of the seagrass biomass in Texas, extensive seagrass meadows characterize the lagoon (Kaldy et al., 2002). *Thalassia testudinum* (turtle grass), *Syringodium filiforme* (manatee grass),

and *Halodule wrightii* (shoal grass) are the most common seagrass species found within the lagoon (Kowalski et al., 2009). The bay is divided into the Upper Laguna Madre, dominated by *H. wrightii* and *S. filiforme*, and the Lower Laguna Madre, which has been trending towards *T. testudinum* dominance since the creation of the Port Mansfield Cut, which allowed for greater exchange between the ocean and the bay, decreasing the overall salinity of the bay (Congdon and Dunton, 2016; Onuf, 2007).

Ecosystem Services of Seagrasses

Seagrass and algae beds are largely considered to be some of the most valuable systems in terms of the ecosystem services that they provide (Costanza et al., 1997). Seagrasses supply as much as 12% of marine net ecosystem production even though seagrass are only present in 0.15% of the ocean floor's total surface area (Duarte and Cebrián, 1996). Biodiversity and faunal density has also been found to be higher in areas vegetated by seagrass compared to unvegetated areas (Hemminga and Durate, 2000). This biodiversity enrichment is worth \$3,500 ha^{-1} yr^{-1} in value for commercial fisheries (McRoy and Helfferich, 1977). A stable isotope analysis by Fry and Parker (1979) found that many estuarine species' diets relied heavily on seagrass. Fish and shrimp were especially dependent on seagrass (Fry and Parker, 1979). Additionally, the structure of seagrass beds provides habitat in bays and estuaries and may even be more important than the plant's primary production in some environments (Kaldy et al., 2002).

Coastal vegetation, such as seagrass, is also considered an ecosystem engineer, with the capability to alter the surrounding environment (Borsje et al., 2010). The capacity of seagrass to absorb wave energy and stabilize sediments in bays and estuaries has been well documented (Borsje et al., 2010). Even in heavily grazed, short canopy patches, seagrass has been shown to

reduce sediment erosion three times more than unvegetated areas (Christianen et al., 2013). Accretion of sediments by seagrasses can even aid in mitigating the effects of sea level rise in coastal communities (Van der Wal and Pye, 2004). Considering the current and imminent climatic changes caused by excess carbon in the atmosphere, perhaps one of the most relevant ecosystem services provided by seagrasses is the ability of these marine plants to sequester carbon.

Carbon Dynamics in Seagrasses

High rates of primary productivity by seagrasses allows for short-term storage in plant biomass for the lifespan of the plant, while anoxic and saline soils slow decomposition, allowing for long-term carbon storage in sediment. Seagrass sediments have been shown in some areas to stay deposited over thousands of years (Mcleod et al., 2011). The rate of carbon sequestration in seagrass beds is second only to mangrove and tidal marsh ecosystems (Mcleod et al., 2011). As seagrasses also trap and accrete matter from the water column, stored carbon in sediment surrounding seagrasses has been found to be at least 50% of external origin (Kennedy et al., 2010). While terrestrial carbon storage is relatively well-documented, submerged carbon stores have not been fully assessed, though estimates place global seagrass carbon storage between 4.2 and 8.4 Pg (10^{15} g) of carbon, which is greater than terrestrial carbon storage and rivals storage in mangrove systems (Fourqurean et al., 2012). There is evidence that different species of seagrasses store carbon at different rates, and that mixed species seagrass beds may store carbon differently than homogeneous seagrass beds (Stankovic et al., 2018). Concerns have been raised that seagrass bed degradation could not only lead to the loss of carbon sinks but also allow for associated sediments to become carbon sources (Fourqurean et al., 2012).

Despite the major benefits of maintaining healthy seagrass communities, many areas worldwide have experienced severe losses in seagrass coverage (Orth et al., 2006). An extensive study by Waycott et al. (2009) found that seagrass cover area has decreased an average of 1.5% yr^{-1} since records began in 1879. The rate of loss has increased in the past 20-30 years, with less than a 1% yr^{-1} loss before 1940 to greater than 5% yr^{-1} loss after 1980 (Waycott et al., 2009). If seagrass coverage loss continues, 299 Tg of stored carbon could be released into the atmosphere (Fourqurean et al., 2012). Valuations of carbon stocks in seagrass meadows estimate that this release of stored carbon and loss of carbon sequestration services could result in a global economic loss of US$1.9 – 13.7 billion yr^{-1} (Pendleton et al., 2012).

Threats to Seagrass Communities

Although natural disasters such as tsunamis or disease outbreaks may disrupt seagrass populations, human activity appears to be the largest driver behind loss of seagrass coverage (Waycott et al., 2009). While seagrass beds can counteract the effects of nutrient loading from upstream waste and fertilizer inputs, heavy enrichment, such as that from industrialized agriculture or aquaculture, can be detrimental to seagrass health (Ralph et al., 2007; Waycott et al., 2009). Coastal development has also encroached on seagrass habitat and increased turbidity, limiting light availability and hence constraining photosynthesis (Orth et al., 2006). Influxes of introduced species and overfishing of apex predators can cause surges in herbivores, which may lead to overgrazing of seagrass meadows (Myers, 2007; Orth et al., 2006). In areas that are shallow and heavily trafficked by boats, as in the Laguna Madre, scarring by boat propellers is a common detriment to seagrass coverage (Fletcher et al., 2009). The far-reaching effects of

climate change will likely only exacerbate these issues and present new threats to seagrass communities (Orth et al., 2006).

Current Seagrass Monitoring Methods

The most prominent current efforts to monitor seagrass coverage in Texas are made by the Texas Seagrass Monitoring Project. These methods rely on satellite imagery from LANDSAT 8 to generate vegetation maps that are then used to draw 500-750 m wide hexagons. Hexagon size is dependent on the size of the system. For the Lower Laguna Madre, 750 m wide hexagons are used. A single point is randomly selected within each hexagon and observations by divers are made within four $0.25m^2$ quadrat at each point. Hexagons are only assigned in ≤ 2 m of water, unless there is evidence of seagrass at greater depths in the area. From this point-based data, seagrass coverage within the hexagon is interpolated using ArcGIS software.

Methods that rely on point-data are the most commonly used mapping techniques worldwide, as few alternatives to this practice currently exist. This method of estimating seagrass coverage is time- and labor-intensive. LANDSAT 8 satellite imagery has a spatial resolution of 30 meters, so smaller bare patches within or surrounding seagrass beds could be easily missed, and small losses from sampling season to sampling season may not be readily apparent. Point data may also result in over- or underestimation of seagrass coverage. Since seagrass density is often not heterogeneous within a given area, any data that only uses areas with >50% coverage can fail to account for areas with scattered coverage.

In order to effectively monitor seagrass ecosystems, management agencies need accurate, repeatable, large-scale mapping techniques that can be completed with limited personnel (Roelfsema et al., 2009). Recent research in resource management emphasizes the need for seascape-scale monitoring and planning (de la Torre-Castro and Rönnbäck, 2004). Remote

sensing provides a versatile way to oversee large portions of landscapes, although the presence of water in coastal ecosystems provides unique challenges. Depth, tidal influence, water clarity, benthic type, and sunglint all influence the ability of sensors to provide valid imagery. One of the most commonly used vegetation indices in terrestrial vegetation mapping is the Normalized Difference Vegetation Index (NDVI). NDVI uses the near-infrared (NIR) wavelength that is more strongly reflected in green vegetation to calculate vegetation coverage. One of the most notable complexities of mapping submerged vegetation is that the NIR wavelength is attenuated in the first few meters of water, depending on water clarity and quality.

The accessibility of multispectral sensors and Unmanned Aerial Vehicles (UAVs) has increased in recent years, promoting innovative uses in seascape management. Spectral imaging is the study of how light reflects from various substances. Multispectral sensors consist of 2-10 distinct bands, each of which represents a portion of the electromagnetic spectrum. Several satellites equipped with multispectral sensors provide organizations with imagery for various mapping purposes, including environmental monitoring. Although satellite data tends to be readily available, satellite-mounted sensors generally produce data that has coarse spectral resolution (i.e., single pixels representing large, often highly variable spatial areas). Close-water remote sensing, such as that supplied by sensors mounted on UAVs, can provide a solution to the issue of spectral resolution presented by satellite data.

Study Objectives

The first objective of this study was to develop reliable methodology to assess seagrass coverage using near-water aerial multispectral sensing techniques by establishing the relationship between spectral reflectance and seagrass canopy coverage. The second goal of this project was

to provide evidence for the link between seagrass coverage and stored below-ground carbon, which has not been adequately studied in seagrass. By establishing the link between belowground carbon storage and canopy coverage while refining the use of near-water multispectral imagery, future studies may be able to better estimate carbon storage using remote sensing.

Hypotheses

Hypothesis I: Distinct spectral signatures will be detectable between fringe seagrass, full seagrass, and bare sediment patches.

a) Vignetting, or the darkening of pixels away from the center of an image, and directional bias from solar interference will cause greater variance across reflectance values.
b) More variance will be explained if factors such as water depth, sediment bulk density, and flight altitudes are considered.
c) Using ratios of bands (wavelengths) or calculated metrics using relationships between bands will produce better models than models using single bands.
d) Extracting reflectance values for the same quadrat across multiple images will produce stronger relationships (i.e., provide better estimates of seagrass cover).
e) NDVI will not be a useful index to predict seagrass cover as NIR and red are quickly attenuated in water.

Hypothesis II: Sedimentary carbon will be higher in areas with more seagrass cover, with the highest sedimentary carbon levels in the shallowest 0-10 cm section of the core and carbon decreasing with depth.

Hypothesis III: Because canopy cover positively relates to belowground carbon storage and spectral reflectance can estimate canopy cover, reflectance values could be used to predict belowground carbon storage, once a baseline has been established for the area.

CHAPTER 2

METHODOLOGY

To investigate the link between reflectance, seagrass cover, and sedimentary carbon a combination of remote sensing and ground-truthing methods were employed (Fig 1).

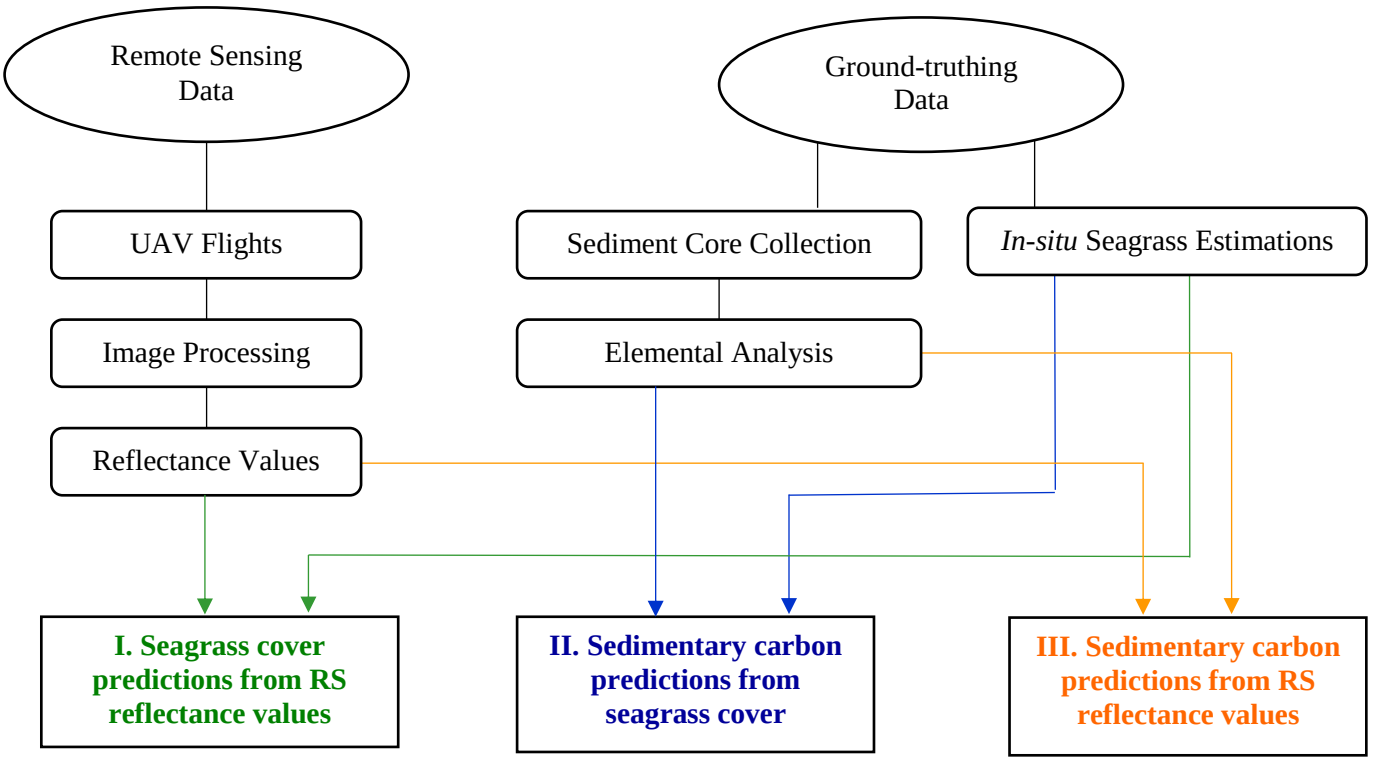

Figure 1: Flow chart of methodology, which included collection of remotely sensed data, in-situ observations, and sediment core collection.

Data Collection

Study Site

The study site was located near the city of South Padre Island, Texas in the Lower Laguna Madre between 26.141106, -97.184133 and 26.137399, -97.179298 (Fig. 2). The depth averaged 75 cm. Tides range from 30-60 cm, with the greatest tidal changes driven by wind, rather than lunar cycle. The climate is subtropical, with average high air temperatures in August of 28.7°C and average low air temperatures in January of 14.7°C. Water temperatures average 14.4°C in winter and 26.6°C in summer, with an average yearly rainfall in the area is 702 mm. Any influx of nutrients or suspended particles into this area comes largely from an agricultural region via the Arroyo Colorado (Onuf, 2007). The site is dominated by *T. testudinum,* with some *H. wrightii* fringing in the shallows. This site was selected for water clarity and variation in seagrass coverage.

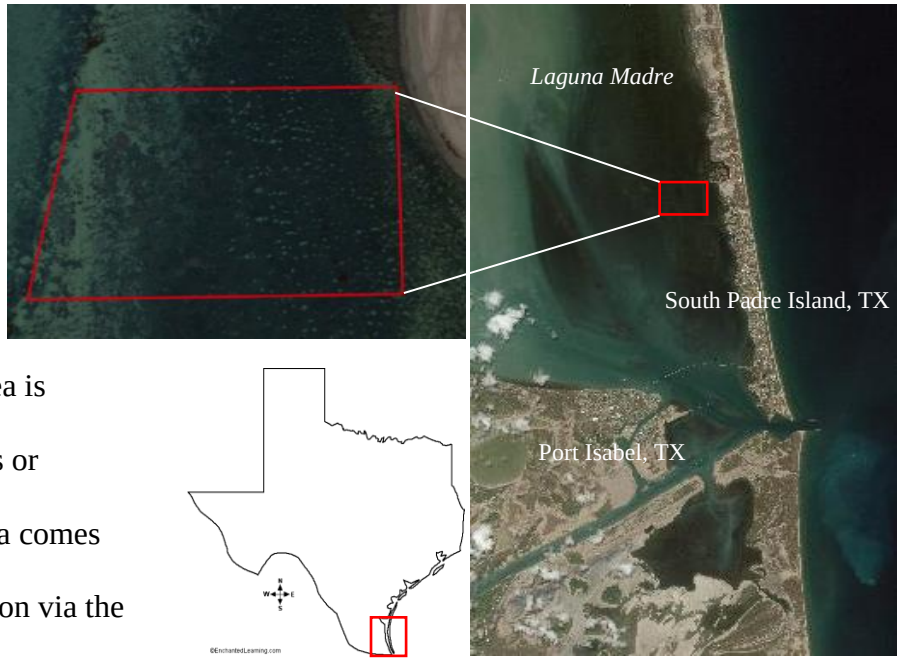

Figure 2: The study site was located near-shore on the Laguna Madre side of mid-South Padre Island.

Ground-truthing

Ground-truthing was used to calibrate our interpretation of the images taken by the drone-mounted multispectral camera. A diver estimated seagrass coverage *in situ* with a series of forty (40) 0.25-m^2 quadrats. Quadrats were located at points previously identified as falling

within one of four coverage categories: bare, gap, fringe, and full. Bare patches were defined as being areas devoid of seagrass beds outside of seagrass patches, while gap areas were smaller patches (generally between 1-3 meters in diameter) without seagrass within a larger seagrass matrix. Fringe seagrass areas were the seagrass areas bordering gaps. The diver estimated the actual canopy cover percentage within each of the quadrats. A total of 10 quadrats were surveyed for each of the four categories.

Remote Sensing

Various multispectral camera setups were tested before the MAIA MV 9-band multispectral camera was found to have the least interference from sunglint. The MAIA camera was designed to be compatible with satellite imagery from WorldView-2 and is capable of detecting wavelengths from 385 to 950 nm. MAIA's Incoming Light Sensor was designed to work with the camera, detecting and correcting variations in incoming solar radiation. The camera was attached to a Matrice 600 PRO unmanned aerial vehicle via a Gremsy T3 gimbal (Figure 3). Multispectral data was collected above the anchored quadrats. Maps Made Easy open-source software was used to design flight paths. Mapping and in-water surveys were completed in mid-October 2018. Flights over bare patches were later added in early March 2019.

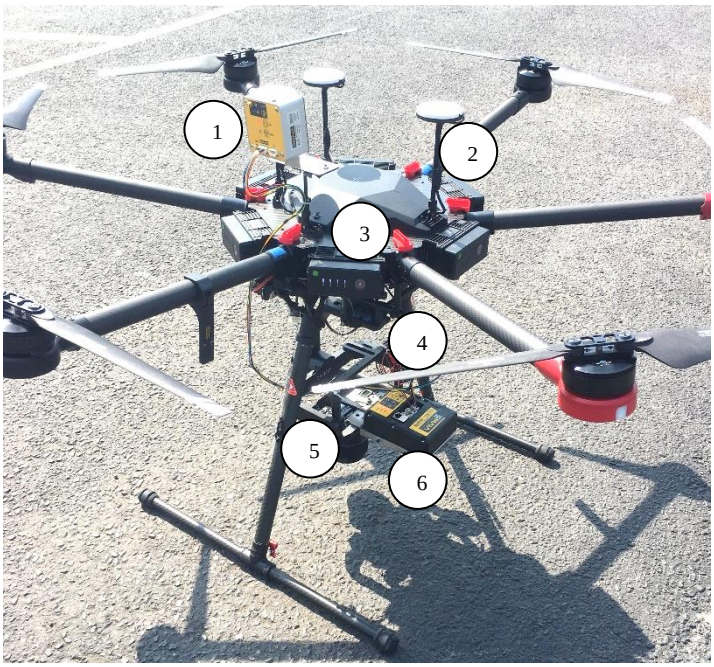

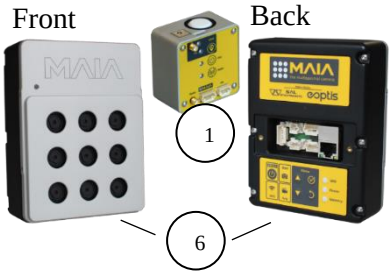

1. MAIA Incoming Light Sensor
2. GPS Units
3. Matrice 600 Pro Drone
4. Gremsy T3 Gimbal
5. Homemade camera mount
6. MAIA WV Multispectral Sensor

Figure 3: Photograph of the UAV, gimbal, and camera setup (left) and images of the MAIA Camera and Incoming Light Sensor (right).

Retrieving Sediment Cores

After imagery was obtained one approximately 30-cm sediment core was extracted within each sampling quadrat, for a total of 40 cores, using a 50 cm x 7.5 cm PVC pipe. A homemade coring device featuring a ball valve to create and release suction was used for the actual core extraction (Fig. 4). The PVC pipes were inserted into the coring device, and the rubber coupling was tightened as much as possible. With the ball valve open, the pipe was inserted by hand into the sediment up to the rubber coupling. A rubber mallet was used to complete the insertion to

Figure 4: Photograph of the homemade coring device used to collect sediment samples.

approximately 40 cm, if necessary. The ball valve was then closed and the entire device was pulled from the soil, with care taken to keep the sample upright. The bottom of the core was then capped using a 7.6 cm U-LINE polyurethane cap. The cores were placed in a freezer at -17°C within 6 hours of collection.

Sample and Data Analysis

Assessment of Carbon Stocks

Once frozen , each core was cut into three 10-cm segments (0-10, 10-20, 20-30 cm). Any deeper segments of sediment were discarded. Cores (n = 120) were processed in accordance with The Blue Carbon Initiative guidelines for assessing coastal blue carbon (Howard et al., 2014). Each sample was weighed and dried at 65°C until no weight change was observed. After dry weight was obtained, several height measurements along the PVC ring were taken and used to calculate a more precise sample volume to account for minor variability in cut locations or cut angles. Each sample was then homogenized using a mortar and pestle. The sample was then passed through a series of sieves with only granules less than 63 μm in size were retained for further processing. The sieves, mortar, and pestle were cleaned between samples using compressed air. Tin capsules were weighed, a small sediment sample (approximately 0.05 mg) was added, and then each capsule was carefully sealed and re-weighed for CHN analysis.

Since the CHNS elemental analyzer (PerkinElmer, Waltham, Massachusetts, USA) quantifies total carbon content, subsamples from each soil sample (n = 120) were weighed, placed into a muffle furnace at 500°C for 3 hours, and then re-weighed to quantify loss on ignition. Organic carbon volatilizes at 500°C, thus only mineral carbon (inorganic C) is left

behind. Combusted and un-combusted paired sets of soil samples were analyzed, which determined the total carbon and nitrogen content of paired sets of samples, and allowed us to quantify inorganic carbon content as well as organic carbon content using two different methods. The first was by subtracting inorganic carbon content (the ashed subsample) from total carbon content (original sample) as measured by the elemental analyzer. The second method aimed to eliminate error margins from the EA by only using the mass lost from a sample after combustion (ashing) in the muffle furnace. This method for finding organic carbon is known as the mass loss on ignition (LOI) method.

Image Processing

The images taken from the multispectral sensors were stitched together using MAIA - MultiCam Stitcher Pro photogrammetry software. GPS locations and drone headings were taken from the sensor's logfile. The latitude and longitudes were converted to UTM. Using the UTM coordinates and drone heading, a MATLAB script was used to generate accurate coordinates for each image. The multichannel images generated by MAIA's software were then georeferenced using ESRI's ArcGIS and the adjusted coordinates. Of the 40 quadrats placed, 37 could be found within the images. Within each quadrat, the centermost nine pixels were selected using the pixel identifier tool in ArcMap. Other pixels within the quadrat were excluded due to bleed from the white PVC of the quadrats into surrounding pixels. The reflectance values for each of the 8 bands from the centermost pixels were then averaged to provide one reflectance value per band per image. This process was repeated using 3 additional images for each quadrat. Quadrat distance from the center of the image was measured to allow us to assess if any darkening of pixels away from the center of the image, also known as the vignetting effect, was present. The

maximum possible reflectance value for a given band in a digital image = 2^n, where n = number of bits; therefore, the raw reflectance values were divided by the maximum possible value to find actual reflectance. Since the original images were taken using a 12-bit camera, the values were divided by 4096 ($2^{12} = 4096$) to find actual reflectance. These values were then multiplied by 100 to find the reflectance percentage for each band. The spectral profiles for each quadrat were then compared to the seagrass coverage estimations made via diver surveys.

Statistical Analysis

The relationships between remotely sensed data, on-the-ground seagrass surveys, and the results of laboratory soil analyses were assessed by fitting a series of generalized linear models. After the remote sensing data was processed, we first considered potential sources of error (noise in our reflectance data) by performing simple and multiple regression analyses to examine the relationships between spectral reflectance values and (a) the distance of sampled pixels from the center of the image (to test for vignetting effects), (b) water depth, (c) flight altitude, and (d) sediment bulk density; and by using ANOVA to examine the relationships between reflectance values and the drone heading's prevailing cardinal direction (to test for directional bias in reflectance strength). Principal Components Analysis (PCA) was performed to examine the multivariate relationships between these potential confounding environmental factors.

To address Hypothesis I, 141 simple regression analyses were performed to examine the relationships between total seagrass coverage values acquired via diver surveys and remotely sensed reflectance data within individual spectral categories and across a broad range of composite spectral indices or ratios. These regressions included considerations of 47 individual spectral bands or indices/ratios for each of three data subsets, namely either (a) one reflectance

value derived from a single image of each quadrat, (b) four reflectance values for each quadrat with one derived from each of the four images captured of each quadrat, or (c) the average of the four reflectance values for each quadrat.

Next, to address Hypothesis II, 12 regression analyses were used to examine relationships between seagrass bed characteristics and Sedimentary carbon content (organic via loss on ignition, and organic, inorganic, and total C via elemental analyzer) at each soil depth (0-10, 10-20, and 20-30 cm depth).

Finally, to address Hypothesis III, we performed three sets of 188 regression analyses to examine the relationships between remotely sensed spectral data and Sedimentary carbon content. This included regressions relating each of the same 47 individual spectral bands or indices/ratios to each of the four Sedimentary carbon response variables (organic via loss on ignition, and organic, inorganic, and total via elemental analyzer), and doing so for each of the three soil layers taken from cores (0-10, 10-20, and 20-30 cm depth) for a total of 564 regressions (47 reflectance metrics × 4 carbon variables × 3 soil depths).

In all cases we considered linear models fit using ordinary least squares regressions, and for models of interest we additionally considered nonlinear (e.g., sigmoidal) models fit using ordinary least squares regressions. Where more than one model was fit for a given set of variables, we identified the function that provided the best goodness of fit based on model R^2 values. Linear regression model fitting and evaluation was conducted using Tableau 2019.1. Nonlinear regression model fitting was performed using SigmaPlot 11. Multiple regressions and PCA were performed using R statistical software version 3.4 via the lm() function in the base package and the rda() function (which performs a PCA if there are no categorical variables) in

the ‘vegan’ package. The rda() function was chosen over the base prcomp() function because of its superior graphing capabilities.

CHAPTER 3

RESULTS

Part I: Prediction of Seagrass Cover from Reflectance Values

Flight Trials

To establish methodology to map submerged vegetation, evaluating altitude and time of day for flights was necessary. Flights were done at both 100 and 50 m. In October, images from the flights at 100 m were used because these had the least interference from sunglint. The second round of flights in March were at 50 m to procure more fine-scale resolution. At 100 m, each image covered an area of approximately 2,466 m^2 and each pixel corresponded to a horizontal distance of ca. 4.5 cm on the ground. At 50 m, each pixel corresponded to a horizontal ground distance of ca. 2.25 cm. March 2019 images were comparable in terms of sunglint, but interference from waves was exacerbated at the lower height. Sunglint was further mitigated by flying within three hours of solar noon.

Spectral Signatures and Seagrass Coverage

Reflectance values were used to predict seagrass cover using single bands, band to band ratios, various band indices, and angles of spectral curves (Table 1). To explore whether better cover predictions could be made using reflectance values from the same quadrat in multiple images, models using 3 additional images were also fit after plotting the reflectance values from

replicate photos of each quadrat as individual points. Finally, average reflectance for each quadrat across the 4 images was used to predict seagrass cover from reflectance (see Methods sections above for more information on model fitting.

Single Image Models. Linear regressions were generated using the reflectance of each of the spectral bands to determine the relationship between reflectance and seagrass cover. Within each quadrat, seagrass coverage was significantly predicted by reflectance values for each spectral band except red-edge and near-infrared. Low R^2 values (≤ 0.342) across single band reflectance indicate that cover predictions using single band reflectance do not explain variance within the model particularly well. Because the purple band was consistent across seagrass cover, and because red-edge band tended to have a negative relationship with the blue, green, orange, and red bands, the purple and red-edge bands were used most often to create ratios and indices.

Ratios of spectral bands showed more significant and stronger relationships with seagrass cover than single bands alone in most instances. Ratios of the purple band to blue, green, orange, and red all had p-values < 0.0001, with R^2 values ranging from 0.366 to 0.474. The linear regression using the ratio of purple to red-edge was borderline significant, with a low R^2 value of 0.097. Of the purple ratios, purple:green and purple:orange predicted seagrass cover most accurately with the least unexplained variance. Averaging the purple ratios also produced a highly significant ($p < 0.0001$) model, with an R^2 value of 0.434. Ratios of the other bands to the red-edge band produced similar results. Of the red-edge ratios, the red-edge:orange model best predicted seagrass cover ($R^2 = 0.406$). Averages of the red-edge ratios also produced highly significant models.

Table 1: Linear relationships between cover and reflectance for various single band reflectance, band ratios, inverse band ratios, reflectance indices, and spectral calculations from single image, multiple images, and averages across 4 images.

*p ≤ 0.051 – 0.06 . p ≤ 0.05 = * p ≤ 0.01 = ** p ≤ 0 .001 = *** p < 0.0001 = ****

Predictor					Single image		4 images		Average of 4 images	
					R^2	P	R^2	P	R^2	P
Single band	Purple				0.219	**	0.179	****	0.240	**
Single band	Blue				0.308	***	0.295	****	0.337	***
Single band	Green				0.342	***	0.322	****	0.356	****
Single band	Orange				0.334	***	0.312	****	0.355	***
Single band	Red				0.283	***	0.275	****	0.324	***
Single band	Red Edge				0.000	ns	0.030	*	0.000	ns
Single band	Near IR				0.000	ns	0.060	**	0.082	.
Ratio	Blue		Purple		0.434	****	0.452	****	0.516	****
Ratio	Green		Purple		0.473	****	0.426	****	0.481	****
Ratio	Orange		Purple		0.474	****	0.437	****	0.497	****
Ratio	Red		Purple		0.366	****	0.377	****	0.444	****
Ratio	Red Edge		Purple		0.097	.	0.159	****	0.267	**
Average	Ratios		Purple		0.434	****	0.402	****	0.451	****
Ratio	Purple		Red Edge		0.123	*	0.161	****	0.260	ns
Ratio	Blue		Red Edge		0.302	***	0.391	****	0.515	***
Ratio	Green		Red Edge		0.382	****	0.414	****	0.527	****
Ratio	Orange		Red Edge		0.406	****	0.451	****	0.592	****
Ratio	Red		Red Edge		0.357	****	0.445	****	0.609	****
Average	Ratios		Red Edge		0.357	****	0.422	****	0.556	****
Inverse band	Green				0.538	****	0.515	****	0.567	****
Inverse ratio	Blue		Purple		0.480	****	0.528	****	0.610	****
Inverse ratio	Blue		Red Edge		0.399	****	0.481	****	0.646	****
Inverse ratio	Red		Red Edge		0.465	****	0.538	****	0.713	****
Inverse average	Ratios		Purple		0.495	****	0.480	****	0.551	****
Inverse average	Ratios		Red Edge		0.464	****	0.515	****	0.676	****
NDVI (Ratio)	Near IR	- Red	/ Near IR	+ Red	0.200	**	0.245	****	0.496	****
Ratio	Near IR	- Red Edge	/ Near IR	+ Red Edge	0.564	****	0.555	****	0.753	****
Ratio	Purple	- Blue	/ Purple	+ Blue	0.461	****	0.497	****	0.556	****
Ratio	Purple	- Green	/ Purple	+ Green	0.528	****	0.483	****	0.562	****
Ratio	Purple	- Orange	/ Purple	+ Orange	0.532	****	0.505	****	0.597	****
Ratio	Purple	- Red	/ Purple	+ Red	0.409	****	0.432	****	0.513	****
Ratio	Purple	- Red Edge	/ Purple	+ Red Edge	0.111	*	0.168	****	0.286	***
Average	Ratios		**Above B G O R RE -/+ V Values**		0.434	****	0.415	****	0.449	****
Ratio	Red Edge	- Purple	/ Red Edge	+ Purple	0.111	*	0.173	****	0.253	****
Ratio	Red Edge	- Blue	/ Red Edge	+ Blue	0.367	****	0.470	****	0.608	****
Ratio	Red Edge	- Green	/ Red Edge	+ Green	0.480	****	0.512	****	0.634	****
Ratio	Red Edge	- Orange	/ Red Edge	+ Orange	0.497	****	0.546	****	0.686	****
Ratio	Red Edge	- Red	/ Red Edge	+ Red	0.428	****	0.526	****	0.684	****
Average	Ratios		**Above V B G O R -/+ RE Values**		0.412	****	0.496	****	0.641	****
Angle	Purple		Blue		0.371	****	0.359	****	0.447	****
Angle	Purple		Green		0.382	****	0.353	****	0.441	****
Angle	Purple		Orange		0.376	****	0.343	****	0.461	****
Sum	Angles		Purple		0.381	****	0.358	****	0.452	****
Angle	Red Edge		Red		0.483	****	0.440	****	0.564	****
Angle	Red Edge		Orange		0.482	****	0.437	****	0.548	****
Angle	Red Edge		Green		0.453	****	0.419	****	0.497	****
Sum	Angles		Red Edge		0.478	****	0.439	****	0.543	****

Several inverse ratios also produced highly significant relationships between seagrass cover and reflectance. The inverse ratio of green reflectance (1/G) was a highly significant predictor of seagrass cover and explained variance well ($R^2 = 0.538$). Additionally, inverse ratios of blue:purple (1/B:P), blue:red-edge (1/B:RE), and red:red-edge (1/R:RE) had p-values of < 0.0001, with R^2 values from 0.399 – 0.495.

NDVI (NIR – R/NIR + R), a commonly used index for terrestrial vegetation, could predict seagrass cover ($p = 0.006$), but the lower R^2 value of 0.200 indicates that our other models are likely better suited for submerged vegetation such as seagrass. A similar index using NIR and red-edge instead of red (NIR – RE/NIR + RE) predicted seagrass cover more accurately and was actually the single best predictor of seagrass cover when using the reflectance values from a single image, with a p-value < 0.0001 and a R^2 value = 0.564.

Purple indices (P – Band / P + Band) also correlated strongly with seagrass cover for blue, green, orange, and red bands (p-values < 0.0001, R^2 values of 0.409 – 0.532). Red-edge indices (RE – band / RE + band) also proved useful in seagrass cover predictions, showing a significant relationship using purple and highly significant relationships for all other bands, but slightly lower R^2 values (0.367–0.497) than the corresponding purple indices.

The angle predictor metrics were calculated by generating an average spectral curve for each cover category. For each category, the angle between the purple and blue, purple and green, and purple and orange was taken. This was repeated for the three bands closest to the red-edge, generating red-edge to red, red-edge to orange, and red-edge to green values. The angles between the purple band and other bands of reflectance curves were also highly significant ($p < 0.0001$) indicators of seagrass cover, although R^2 values were relatively low (0.371 – 0.382). The angles

of red-edge to other bands produced better seagrass cover models, with p-values < 0.0001 and R^2 values $\geq$ 0.453.

Multiple Image Models. Single band reflectance for purple, blue, green, orange, and red also showed significant relationships with seagrass cover when taken from 4 images, although these were relatively weakly correlated (R^2 values ≤ 0.322). Red-edge and NIR relationships were significant but explained far less variance than other bands (R^2 = 0.030 and 0.060, respectively).

Purple ratios (Band:P) all produced p-values < 0.0001 with R^2 values ranging from 0.159 for red-edge:purple to 0.452 for blue:purple. Red-edge ratios (Band:RE) had similar results, with low p-values (< 0.0001) and comparable R^2 values (0.161–0.451). The band:red-edge and band:purple averaged ratios also produced similarly low p-values, with R^2 values of 0.422 and 0.402, respectively. Relationships between seagrass cover and the inverse ratios of 1/G, 1/B:P, 1/B:RE, 1/R:RE were highly significant and had R^2 values comparable to when the single-image data subset was used. Of the inverse ratio models, 1/B:P and 1/R:RE had the least unexplained variance (R^2 values = 0.528 and 0.538, respectively).

NDVI was more closely correlated with seagrass cover ($p < 0.0001$, R^2 = 0.245) when using multiple images than when only single image values were used, although the R^2 value for this index remained low. The similar index that used red-edge in place of red again showed a strong correlation with seagrass cover, with relatively less unexplained variance (R^2 = 0.555). As with the single-image data subset, this was the reflectance metric that best predicted seagrass cover (based on its R^2) within the 4-image data subset.

Indices using the purple band produced significant correlations across all bands, with the index using red-edge (P – RE/ P + RE) explaining the least variance (R^2 = 0.168) and the index

using orange (P – O/ P + O) explaining the most (R^2 = 0.505). Red-edge indices had less unexplained variance when using multiple images than when using reflectance values from a single image. Of the red-edge indices, the models using orange (RE – O/ RE + O) and red (RE – R / RE + R) explained the most variance (R^2 = 0.543 and 0.526, respectively), while the model using purple (RE – P/ RE + P) explained the least (R^2 = 0.173).

The models using the angle of purple to other bands were all significantly correlated with seagrass cover, although relatively weakly (R^2 = 0.343 – 0.359). All of the models using red-edge angles showed significant correlations with seagrass cover, with modestly higher R^2 values (0.419 – 0.440). R^2 values for both the purple and red-edge angle models were similar when using either multiple or single-image data subsets, but were consistently slightly lower when using multiple images.

Average Reflectance from Multiple Images. Using the averages of single band reflectance values from four images produced similar statistical significance as using reflectance from a single image and generally reduced significance when compared to using multiple images, but models using average reflectance values typically explained more variance. Only the reflectance from the green band was significantly correlated with seagrass cover in the single band average models ($p < 0.0001$). R^2 values remained consistently low (≤ 0.356) across all single band models using averages.

Averages of simple purple ratios produced highly significant models ($p < 0.0001$), excluding red-edge:purple. The average of these average band to purple ratios also generated a highly significant relationship, with a relatively high R^2 value of 0.451. Averages of the red-edge ratios had highly significant relationships with seagrass cover for all bands except red-edge:

purple, which had no significant relationship. Of these ratios, orange:red-edge and red:red-edge explained the most variance (R^2 = 0.592 and 0.609, respectively). Averaging these averages of red-edge ratios derived from multiple images produced high significance and a R^2 value of 0.556.

The inverse of purple and red-edge ratios had the same high significance across single image, multiple image, and multiple image average models, although the multiple image average models consistently had the highest R^2 values. Of these, the 1/red:red-edge model explained the most variance (R^2 = 0.713), and was one of the models that best predicted seagrass cover overall.

The NDVI model was improved by averaging multiple photos ($p < 0.0001$ and R^2 = 0.496), as was the modified index using red-edge in place of red. NIR − RE / NIR + RE had the least unexplained variance of any model considered and was highly significantly correlated to seagrass cover. In other words, it was the single best predictor of seagrass cover compared to all of the other reflectance metrics. All of the models using purple (P − band/ P + band) and red-edge (RE − band/ RE + band) indices were improved in the multi-image average models. All red-edge index models using reflectance averages had R^2 values ≥ 0.608, except purple which had a low R^2 value of 0.253.

Multi-image averages slightly improved R^2 values across all models using reflectance angles. All angle models remained highly significant. Red-edge angle models had the least unexplained variance, with R^2 values from 0.497 for red-edge:green to 0.564 for red-edge:red.

Confounding Factors

Vignetting. The vignetting effect refers to the reduction of pixel brightness away from the center of an image, resulting in objects near the edge of the image appearing darker than objects near the center. Often, vignetting can be attributed to optical limitations within a camera lens. To correct for this, reflectance values from within the same quadrats at 4 varying distances away from the center of the images were extracted. We found no significant difference in band reflectance at a flight altitude of 100 m (Flight 1) for all bands except red-edge (Fig. 5). For the second flight (flight altitude = 50 m), reflectance values increased for all bands except NIR 1 and NIR 2. This increase could not be attributed to the

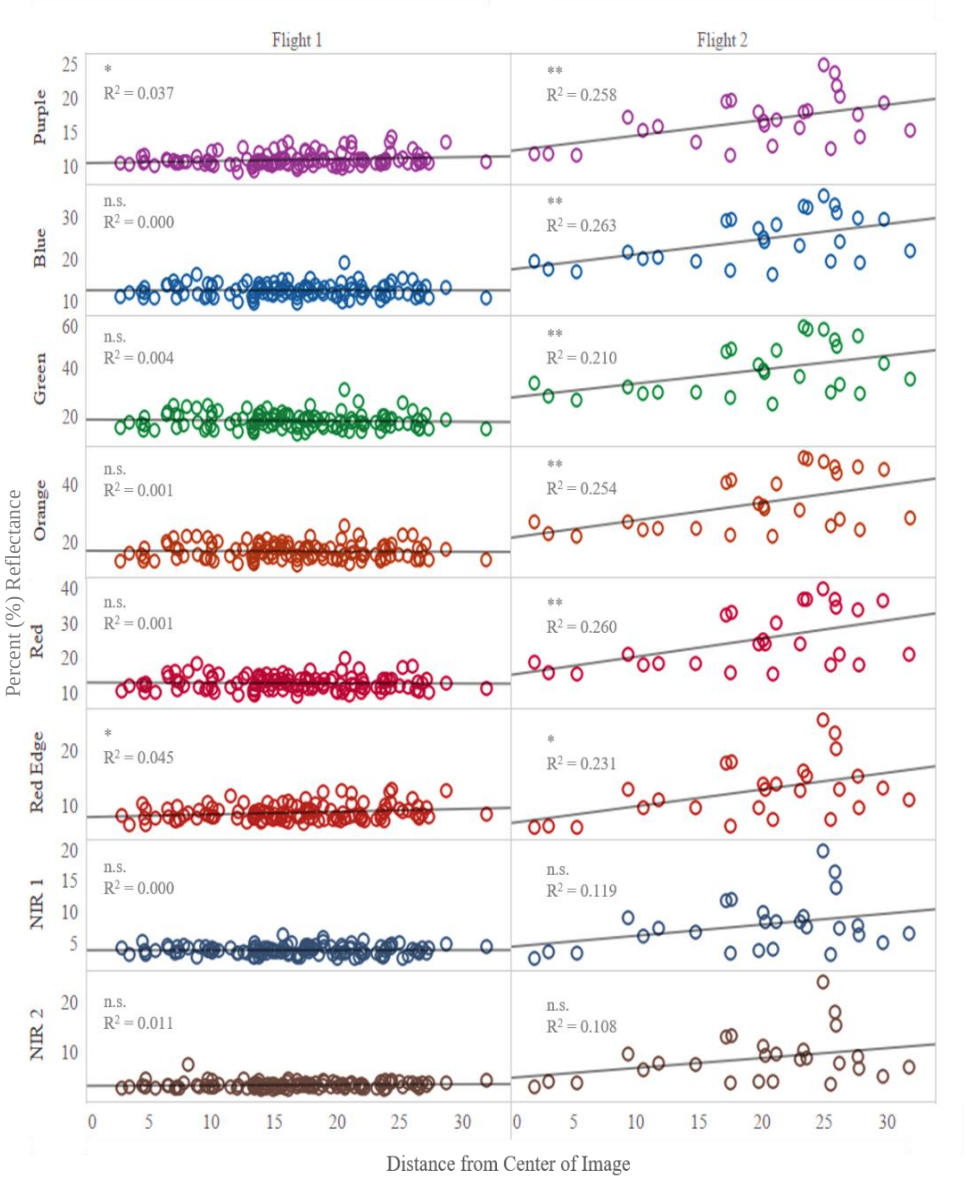

Figure 5: Reflectance values are either not influenced by distance (flight 1, left) or increase (flight 2, right) from the center of the image. This cannot be attributed to the vignetting effect.

p ≤ 0.05 = * *p* ≤ 0.01 = ** *p* ≤ 0 .001 = *** *p* < 0.0001 = ****

vignetting effect. As R^2 values were low for all (≤ 0.263), distance from center of image was not a compelling factor in assessing the relationship between reflectance and seagrass coverage. As differences were consistent across wavelengths for a given flight day, we used band ratios rather than single bands to improve our models.

Directional bias from sun angle. As sunlight was entering the water column from southeast of the study area at the time of collection, the images appeared to be brightest in the southeast corner. To account for any variance that this may have caused in reflectance values, each quadrat's general position within the image was recorded for the 4 images sampled. Directional

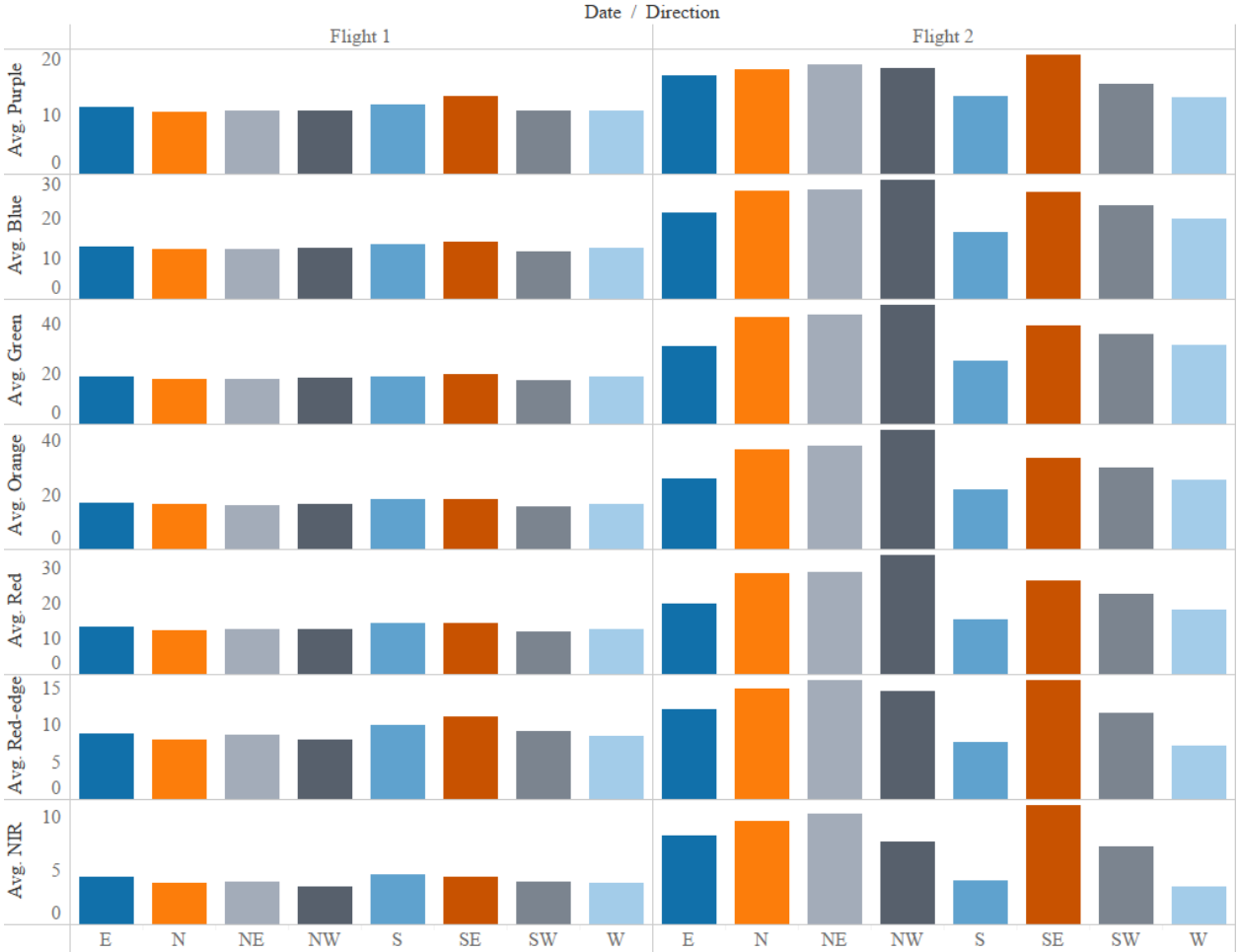

Figure 6: Location of quadrat within the image causes a bias in reflectance values. This bias differs across flight days but is consistent across a given wavelength.

bias was seen in quadrats in both of the flight days (Fig. 6). This bias was more pronounced in the second flight images, which was at a lower altitude (approximately 50 m). Which directions had more bias to reflection varied by flight day. As this bias was consistent across wavelengths, using ratios of bands to each other (as opposed to single band reflectance values) helped to remedy the issue.

Other considerations. Other factors can affect reflectance values. In addition to accounting for distance from center of the image and directional bias from solar angle, we also explored the effects of flight altitude, soil bulk density, and water depth on reflectance values (Fig. 7).

On the first flight day, the effect of water depth was apparent across all wavelengths, except purple. Blue, green, orange, and red bands all had weak but significant positive correlations with water depth ($R^2 = 0.088 – 0.175$). Red-edge and NIR bands were negatively correlated with water depth, although variance was not well explained by the model (R^2 values = 0.109 and 0.080, respectively). On the second flight day, purple was weakly negatively correlated with water depth ($p = 0.018$, $R^2 = 0.203$), but the blue, green, orange and red bands showed no significant relationship. Red-edge and NIR reflectance values were both negatively correlated with water depth, with p-values ≤ 0.05. R^2 values of 0.191 and 0.227, respectively) on the second flight day.

On the first flight day, flight altitude, which ranged from 96 to 100 m, had no effect on reflectance values. At the lower flight altitude (34-42 m) on the second flight day, all reflectance bands were affected by flight height. Reflectance for each band showed a negative correlation with altitude, with R^2 values of 0.271 – 0.578. Green, orange, and red bands had the strongest correlations ($p < 0.001$) with the most explained variance ($R^2 = 0.527 – 0.578$).

Sediment bulk density did not have any effect on reflectance values on the first flight day. On the second flight day, bulk density showed borderline significance with red-edge reflectance ($p = 0.058$, $R^2 = 0.136$) and some correlation with the purple band ($p = 0.031$, $R^2 = 0.173$). All other bands from the second flight day did not appear to be affected by sediment bulk density.

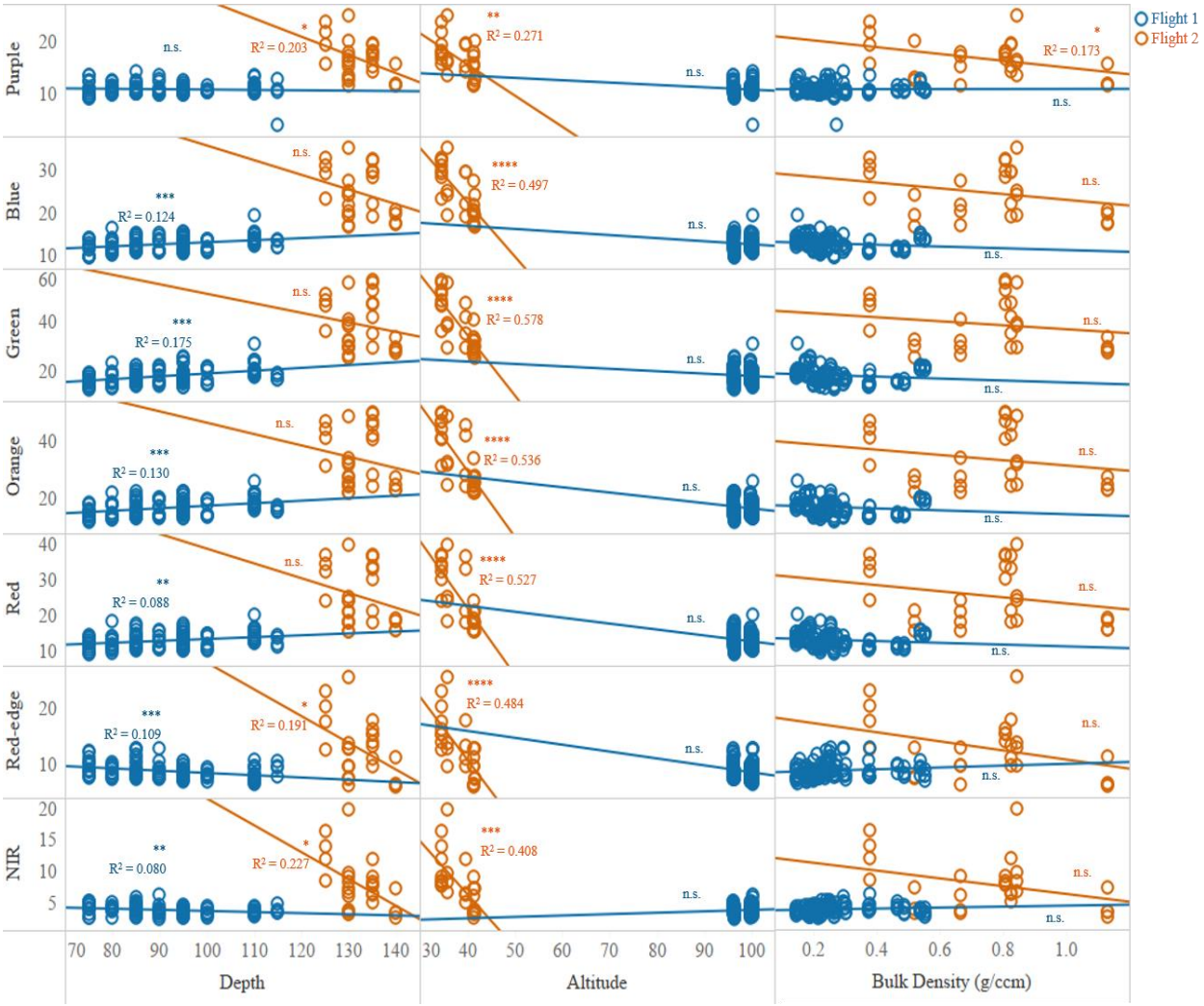

Figure 7: Confounding factors across the 2 flight days. Reflectance across wavelengths was affected by water depth, flight altitude, and sediment bulk density.
*$p \leq 0.05$ = * $p \leq 0.01$ = ** $p \leq 0.001$ = *** $p < 0.0001$ = ****

II. Seagrass Cover and Belowground Stored Carbon

The second goal of this study was to explore the link between seagrass cover and belowground stored carbon (Table 2). Linear and sigmoidal relationships were used to analyze this suspected association. Organic carbon from both mass loss on ignition (LOI) and elemental analysis, as well as inorganic and total C from elemental analysis, were examined from each cover category for the top (0-10 cm), middle (10-20 cm), and bottom (20-30 cm) layers of sediment (Table 3). As quadrats from the gap produced outliers, models were also generated that excluded the gap category.

Table 2: Average percent (%) total carbon, inorganic carbon, and organic carbon for seagrass cover categories for the top 10 cm, middle 10 cm, and bottom 10 cm of sediment collected.

Category	Layer	Total C (%)	C_{inorg} (%)	C_{org} (%) (via EA)	C_{org} (via % mass LOI)
Full	Top	5.419	1.755	3.664	0.110
	Mid	5.375	1.737	3.638	0.110
	Bottom	5.362	1.735	3.627	0.110
Fringe	Top	5.501	1.850	3.651	0.111
	Mid	5.444	1.825	3.619	0.110
	Bottom	5.429	1.820	3.609	0.110
Gap	Top	5.508	1.850	3.658	0.111
	Mid	5.473	1.850	3.623	0.110
	Bottom	5.422	1.819	3.603	0.110
Bare	Top	4.058	1.193	2.865	0.086
	Mid	3.819	1.144	2.674	0.081
	Bottom	3.800	1.155	2.644	0.081

Table 3: Linear and sigmoidal relationships between sedimentary carbon and seagrass cover.
*p ≤ 0.051 – 0.06 . p ≤ 0.05 = * p ≤ 0.01 = ** p ≤ 0 .001 = *** p < 0.0001 = ****

Core depth	Data group	Model type	Mass LOI (%)		Organic C		Inorganic C		Total C	
			R^2	P	R^2	P	R^2	P	R^2	P
0-10 cm	All quadrats	Linear	0	ns	0	ns	0	ns	0	ns
		Sigmoidal	0	ns	0	ns	0	ns	0	ns
	Gaps excluded	Linear	0.225	**	0.103	.	0.202	*	0.191	*
		Sigmoidal	0.307	*	0.185	.	0.278	*	0.295	*
10-20 cm	All quadrats	Linear	0	ns	0.098	*	0.106	*	0.120	*
		Sigmoidal	0	ns	0	ns	0	ns	0	ns
	Gaps excluded	Linear	0	ns	0	ns	0	ns	0	ns
		Sigmoidal	0	ns	0	ns	0	ns	0	ns
20-30 cm	All quadrats	Linear	0	ns	0	ns	0	ns	0	ns
		Sigmoidal	0	ns	0	ns	0	ns	0	ns
	Gaps excluded	Linear	0	ns	0	ns	0.323	**	0	ns
		Sigmoidal	0	ns	0	ns	0	ns	0	ns

Models Using All Quadrats. Few of the models generated using all coverage categories (bare, fringe, gap, and full) produced significant results. Organic, inorganic, and total carbon in the middle (10-20 cm) layer was weakly correlated to seagrass cover in the linear model ($p \leq 0.05$) but low R^2 values (0.098 – 0.120) indicate that these models do not explain variance well.

Models Excluding Gaps. Models that excluded the gap cover category indicated a more significant relationship between cover and sedimentary carbon (Fig. 8). Both linear and sigmoidal relationships were significant or borderline significant across all carbon metrics but only in the top layer of sediment. Seagrass cover's relationships to EA-derived organic carbon in the top 10 cm of sediment were the only borderline significant relationships. The relationship between organic carbon from mass LOI, inorganic carbon and total carbon was best explained by the sigmoidal models, with R^2 values of 0.307, 0.278, and 0.295, respectively.

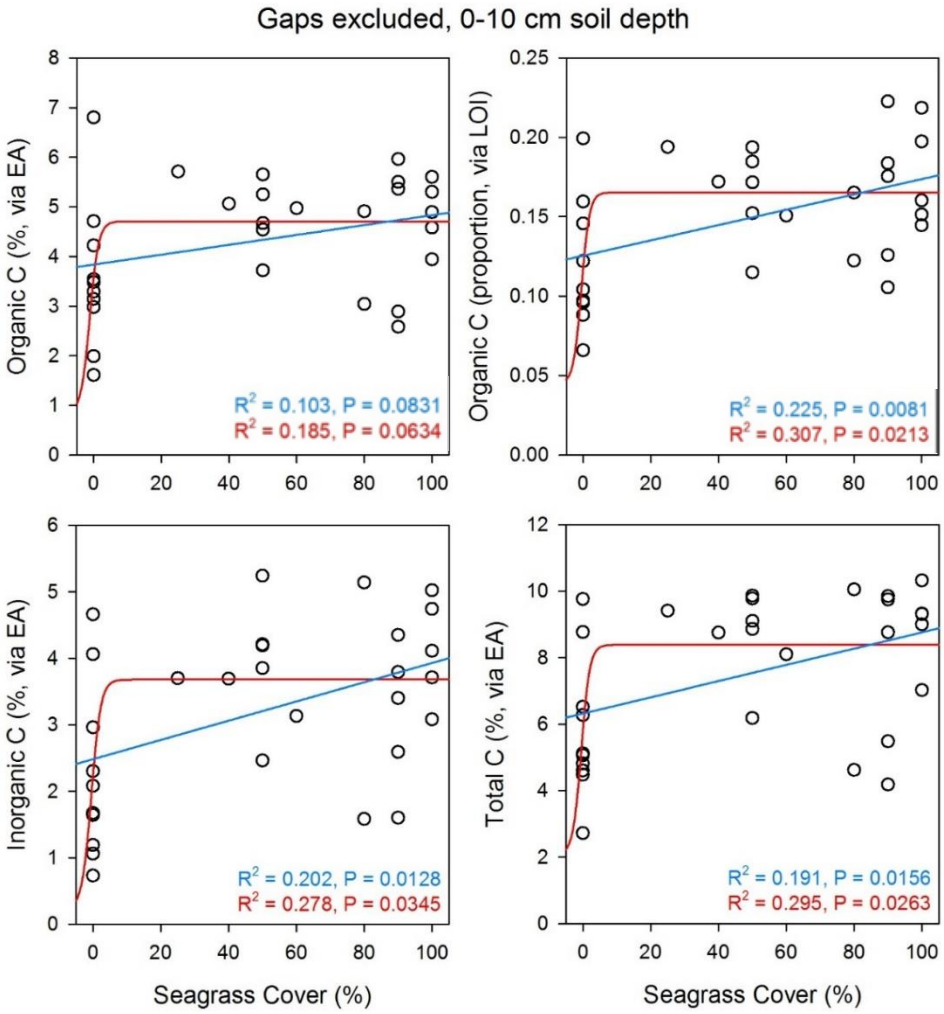

Figure 8: Linear and sigmoidal relationships between seagrass cover and sedimentary carbon when the gap category of cover (outliers) is excluded.

III. Predicting Belowground Stored Carbon from Spectral Reflectance

As we theorized that reflectance could predict seagrass cover and that seagrass cover could predict belowground stored carbon, we also speculated that reflectance could also be used to predict sedimentary carbon. As seagrass cover and belowground stored carbon relationships were stronger when the gap category was excluded, models were generated that excluded the gap category for this hypothesis as well. As sediment depth greatly influenced the reliability of these models, results are discussed by sediment layer.

Carbon Predictions in the Top Sediment Layer

Models Using All Cover Categories. Reflectance from the purple band was a better predictor of organic carbon storage from elemental analysis and from mass LOI ($p \leq 0.001$, $R^2 = 0.299$ and 0.298, respectively). Other single bands were also relatively good predictors of organic carbon storage (Table 4). Predictions of sedimentary organic carbon were also strongly correlated with the angles from the reflectance curves of red-edge:green, purple:blue, and purple:green ($p \leq 0.01$, $R^2 = 0.258$, 0.252 and 0.245, respectively) for organic carbon derived from mass LOI.

Table 4: The relationship of different reflectance band combinations on belowground stored carbon in the upper sediment layer (0-10 cm).
*p ≤ 0.051 – 0.06 . p ≤ 0.05 = * p ≤ 0.01 = ** p ≤ 0 .001 = *** p < 0.0001 = ****

Predictor	0-10 cm															
	All data								Gaps excluded							
	Mass LOI (%)		Organic C		Inorganic C		Total C		Mass LOI (%)		Organic C		Inorganic C		Total C	
	R^2	P	R^2	P	R^2	P	R^2	P	R^2	P	R^2	P	R^2	P	R^2	P
Purple	0.299	***	0.298	***	0.093	.	0.259	**	0.318	**	0.396	***	0.112	.	0.282	**
Blue	0.293	***	0.248	**	0.133	*	0.268	**	0.368	***	0.392	***	0.200	*	0.353	**
Green	0.274	***	0.228	**	0.137	*	0.260	**	0.371	***	0.390	***	0.220	*	0.367	***
Orange	0.242	**	0.211	**	0.112	*	0.228	**	0.330	**	0.366	***	0.180	*	0.324	**
Red	0.233	**	0.221	**	0.093	.	0.216	**	0.304	**	0.360	***	0.148	*	0.296	**
Red Edge	0.178	**	0.270	***	0.026	ns	0.163	*	0.124	.	0.255	**	0.009	ns	0.106	.
NIR	0.231	**	0.297	***	0.052	ns	0.212	**	0.192	*	0.348	**	0.035	ns	0.181	*
B:P	0.183	**	0.087	.	0.145	*	0.168	*	0.350	**	0.243	**	0.306	**	0.340	**
G:P	0.165	*	0.087	.	0.140	*	0.165	*	0.376	***	0.286	**	0.332	**	0.383	***
O:P	0.110	*	0.055	ns	0.093	.	0.107	*	0.294	**	0.231	*	0.246	**	0.296	**
R:P	0.095	.	0.061	ns	0.060	ns	0.088	.	0.234	*	0.201	*	0.172	*	0.230	*
RE:P	0.007	ns	0.001	ns	0.022	ns	0.005	ns	0.101	ns	0.057	ns	0.131	.	0.113	.
Avg(P ratios)	0.132	*	0.075	.	0.101	.	0.129	*	0.287	**	0.225	*	0.235	*	0.285	**
P:RE	0.036	ns	0.000	ns	0.056	ns	0.023	ns	0.189	*	0.079	ns	0.238	**	0.186	*
B:RE	0.164	*	0.047	ns	0.156	*	0.140	*	0.441	***	0.274	**	0.441	***	0.439	***
G:RE	0.166	*	0.058	ns	0.160	*	0.152	*	0.466	****	0.314	**	0.457	***	0.475	****
O:RE	0.129	*	0.037	ns	0.132	*	0.115	*	0.434	***	0.294	**	0.421	***	0.441	***
R:RE	0.123	*	0.041	ns	0.110	*	0.106	*	0.425	***	0.301	**	0.390	***	0.428	***
Avg(RE ratios)	0.142	*	0.042	ns	0.140	*	0.124	*	0.441	***	0.289	**	0.434	***	0.446	***
1/G	0.235	**	0.162	*	0.110	*	0.196	**	0.445	***	0.409	***	0.255	**	0.402	***
1/B:P	0.157	*	0.077	.	0.123	*	0.145	*	0.391	***	0.307	**	0.332	**	0.396	***
1/B:RE	0.097	.	0.019	ns	0.108	*	0.082	.	0.396	***	0.258	**	0.400	***	0.405	***
1/R:RE	0.069	ns	0.017	ns	0.062	ns	0.054	ns	0.353	**	0.262	**	0.313	**	0.356	**
1/Avg(P ratios)	0.110	*	0.065	ns	0.080	.	0.106	*	0.322	**	0.283	**	0.250	**	0.329	**
1/Avg(RE ratios)	0.081	.	0.017	ns	0.089	.	0.068	ns	0.381	***	0.262	**	0.372	***	0.391	***
NDVI	0.011	ns	0.045	ns	0.003	ns	0.009	ns	0.059	ns	0.006	ns	0.161	*	0.074	ns
NIR-RE/NIR+RE	0.087	.	0.024	ns	0.079	.	0.071	ns	0.384	***	0.280	**	0.345	**	0.387	***
P-B/P+B	0.174	*	0.087	.	0.137	*	0.162	*	0.390	***	0.297	**	0.333	**	0.391	***
P-G/P+G	0.139	*	0.072	ns	0.114	*	0.135	*	0.386	***	0.315	**	0.329	**	0.399	***
P-O/P+O	0.090	.	0.045	ns	0.074	ns	0.086	.	0.309	**	0.262	**	0.248	**	0.315	**
P-R/P+R	0.082	.	0.055	ns	0.048	ns	0.075	ns	0.258	**	0.241	**	0.180	*	0.258	**
P-RE/P+RE	0.019	ns	0.001	ns	0.040	ns	0.012	ns	0.154	*	0.068	ns	0.201	*	0.158	*
Avg(P-/P+)	0.106	*	0.071	ns	0.072	ns	0.104	.	0.269	**	0.243	**	0.200	*	0.272	**
RE-P/RE+P	0.019	ns	0.001	ns	0.040	ns	0.012	ns	0.154	*	0.068	ns	0.201	*	0.158	*
RE-B/RE+B	0.120	*	0.028	ns	0.126	*	0.102	.	0.420	***	0.268	**	0.422	***	0.424	***
RE-G/RE+G	0.110	*	0.031	ns	0.115	*	0.098	.	0.422	***	0.296	**	0.410	***	0.436	***
RE-O/RE+O	0.082	.	0.018	ns	0.090	.	0.070	ns	0.386	***	0.270	**	0.369	***	0.394	***
RE-R/RE+R	0.087	.	0.024	ns	0.079	.	0.071	ns	0.384	***	0.280	**	0.345	**	0.387	***
Avg(RE-/RE+)	0.092	.	0.019	ns	0.100	.	0.077	.	0.397	***	0.265	**	0.391	***	0.405	***
Angle PB	0.252	**	0.179	**	0.154	*	0.242	**	0.376	***	0.350	**	0.273	**	0.382	***
Angle PG	0.245	**	0.189	**	0.144	*	0.241	**	0.372	***	0.369	***	0.256	**	0.381	***
Angle PO	0.196	**	0.157	*	0.110	*	0.193	**	0.312	**	0.327	**	0.203	*	0.321	**
Sum(P angles)	0.237	**	0.179	**	0.140	*	0.231	**	0.361	***	0.354	**	0.250	**	0.369	***
Angle RER	0.199	**	0.138	*	0.118	*	0.186	**	0.365	***	0.348	**	0.257	**	0.370	***
Angle REO	0.219	**	0.149	*	0.135	*	0.207	**	0.377	***	0.355	**	0.266	**	0.380	***
Angle REG	0.258	**	0.177	**	0.162	*	0.247	**	0.416	***	0.382	***	0.302	**	0.420	***
Sum(RE angles)	0.222	**	0.153	*	0.136	*	0.210	**	0.384	***	0.361	***	0.273	**	0.389	***

Total carbon was best predicted by the blue, green, and purple ($p \leq 0.001$, $R^2 = 0.268$, 0.260, and 0.259, respectively). The angles from the reflectance curves of red-edge:green, purple:blue, and purple:green were also significantly correlated ($p \leq 0.01$) with total belowground stored carbon. Only three models showed high significant ($p < 0.0001$) for reflectance correlations with organic carbon storage, although those were different for the two methods used to derive organic carbon and R^2 values were low (0.270-0.299), indicating unexplained variance in the models. No models indicated a highly significant relationship between reflectance and inorganic carbon storage. The relationship between reflectance values from 15 different models and total carbon had p-values of ≤ 0.001, but R^2 values were also low (≤ 0.268).

Models Excluding Gaps. When the gap cover category was excluded, our models improved. For organic carbon derived via mass LOI, 27 reflectance combinations had a highly significant relationship, with higher R^2 values (0.361 – 0.466) than all other models that included gaps. Green:red-edge (G:RE) was the most highly significant predictor of organic C (via mass LOI), inorganic carbon, and total carbon ($R^2 = 0.466$, 0.457, and 0.475, respectively, while the relationship of organic carbon derived from the EA was best predicted by 1/green ($p = 0.0003$, $R^2 = 0.409$). A total of 26 band combinations demonstrated a highly significant relationship with total carbon, with $R^2 = 0.367 – 0.475$). Inorganic carbon had a highly significant relationship with 11 different band combinations ($R^2 = 0.369 – 0.457$).

Carbon Predictions in the Lower Sediment Layers

Both the complete data models and the gap-exclusive data models showed little correlation between reflectance and belowground stored carbon for the lower layers of sediment.

In the 10-20 cm layer, NDVI was weakly correlated with organic carbon mass LOI ($p \leq 0.05$, $R^2 = 0.134$) and showed a borderline significant relationship with organic carbon from the EA, inorganic carbon, and total carbon, with low R^2 values (0.098, 0.075, and 0.092, respectively) (Table 5). In the 20-30 cm layer, 14 models (all using some ratio of red-edge) showed borderline significance with inorganic carbon, though low R^2 values (0.109 – 0.143) indicate high variance within the models (Table 6). No other relationships were found.

Table 5: The relationship of different reflectance band combinations on belowground stored carbon in the middle sediment layer (10-20 cm).

p ≤ 0.051 – 0.06 . *p ≤ 0.05 = ** *p ≤ 0.01 = *** *p ≤ 0 .001 = **** *p < 0.0001 = *****

Predictor	10-20 cm															
	All data								Gaps excluded							
	Mass LOI (%)		Organic C		Inorganic C		Total C		Mass LOI (%)		Organic C		Inorganic C		Total C	
	R^2	P	R^2	P	R^2	P	R^2	P	R^2	P	R^2	P	R^2	P	R^2	P
Purple	0.039	ns	0.014	ns	0.025	ns	0.025	ns	0.027	ns	0.000	ns	0.007	ns	0.002	ns
Blue	0.029	ns	0.008	ns	0.020	ns	0.018	ns	0.031	ns	0.000	ns	0.021	ns	0.008	ns
Green	0.023	ns	0.005	ns	0.019	ns	0.016	ns	0.028	ns	0.000	ns	0.025	ns	0.009	ns
Orange	0.017	ns	0.004	ns	0.016	ns	0.013	ns	0.018	ns	0.000	ns	0.023	ns	0.007	ns
Red	0.017	ns	0.004	ns	0.015	ns	0.013	ns	0.016	ns	0.000	ns	0.016	ns	0.004	ns
Red Edge	0.068	ns	0.038	ns	0.042	ns	0.046	ns	0.035	ns	0.003	ns	0.000	ns	0.002	ns
NIR	0.075	ns	0.034	ns	0.043	ns	0.046	ns	0.046	ns	0.003	ns	0.000	ns	0.002	ns
B:P	0.012	ns	0.005	ns	0.006	ns	0.007	ns	0.050	ns	0.020	ns	0.053	ns	0.050	ns
G:P	0.006	ns	0.001	ns	0.006	ns	0.005	ns	0.033	ns	0.009	ns	0.055	ns	0.037	ns
O:P	0.001	ns	0.000	ns	0.002	ns	0.001	ns	0.015	ns	0.009	ns	0.048	ns	0.034	ns
R:P	0.001	ns	0.000	ns	0.002	ns	0.001	ns	0.013	ns	0.009	ns	0.028	ns	0.024	ns
RE:P	0.056	ns	0.062	ns	0.028	ns	0.042	ns	0.026	ns	0.040	ns	0.007	ns	0.009	ns
Avg(P ratios)	0.007	ns	0.003	ns	0.006	ns	0.006	ns	0.031	ns	0.015	ns	0.044	ns	0.039	ns
P:RE	0.019	ns	0.024	ns	0.015	ns	0.020	ns	0.000	ns	0.006	ns	0.018	ns	0.000	ns
B:RE	0.000	ns	0.003	ns	0.000	ns	0.001	ns	0.017	ns	0.000	ns	0.054	ns	0.019	ns
G:RE	0.000	ns	0.002	ns	0.000	ns	0.000	ns	0.018	ns	0.001	ns	0.059	ns	0.022	ns
O:RE	0.004	ns	0.007	ns	0.001	ns	0.003	ns	0.006	ns	0.000	ns	0.059	ns	0.019	ns
R:RE	0.007	ns	0.010	ns	0.002	ns	0.004	ns	0.003	ns	0.000	ns	0.046	ns	0.012	ns
Avg(RE ratios)	0.002	ns	0.006	ns	0.001	ns	0.002	ns	0.009	ns	0.000	ns	0.054	ns	0.017	ns
1/G	0.003	ns	0.000	ns	0.002	ns	0.001	ns	0.019	ns	0.001	ns	0.028	ns	0.013	ns
1/B:P	0.000	ns	0.001	ns	0.000	ns	0.000	ns	0.020	ns	0.003	ns	0.050	ns	0.025	ns
1/B:RE	0.019	ns	0.026	ns	0.012	ns	0.018	ns	0.001	ns	0.002	ns	0.044	ns	0.006	ns
1/R:RE	0.032	ns	0.032	ns	0.018	ns	0.025	ns	0.001	ns	0.003	ns	0.026	ns	0.002	ns
1/Avg(P ratios)	0.000	ns	0.001	ns	0.000	ns	0.000	ns	0.011	ns	0.003	ns	0.038	ns	0.020	ns
1/Avg(RE ratios)	0.025	ns	0.031	ns	0.014	ns	0.021	ns	0.000	ns	0.004	ns	0.038	ns	0.004	ns
NDVI	0.134	*	0.098	.	0.075	ns	0.092	.	0.050	ns	0.023	ns	0.027	ns	0.000	ns
NIR-RE/NIR+RE	0.021	ns	0.024	ns	0.011	ns	0.016	ns	0.000	ns	0.002	ns	0.033	ns	0.005	ns
P-B/P+B	0.002	ns	0.000	ns	0.001	ns	0.001	ns	0.029	ns	0.007	ns	0.052	ns	0.033	ns
P-G/P+G	0.000	ns	0.001	ns	0.000	ns	0.000	ns	0.016	ns	0.001	ns	0.047	ns	0.020	ns
P-O/P+O	0.002	ns	0.002	ns	0.000	ns	0.001	ns	0.005	ns	0.003	ns	0.042	ns	0.021	ns
P-R/P+R	0.001	ns	0.001	ns	0.000	ns	0.000	ns	0.004	ns	0.003	ns	0.023	ns	0.014	ns
P-RE/P+RE	0.038	ns	0.043	ns	0.024	ns	0.033	ns	0.007	ns	0.018	ns	0.014	ns	0.001	ns
Avg(P-/P+)	0.001	ns	0.000	ns	0.002	ns	0.001	ns	0.016	ns	0.007	ns	0.034	ns	0.025	ns
RE-P/RE+P	0.038	ns	0.043	ns	0.024	ns	0.033	ns	0.007	ns	0.018	ns	0.014	ns	0.001	ns
RE-B/RE+B	0.009	ns	0.016	ns	0.006	ns	0.010	ns	0.004	ns	0.001	ns	0.049	ns	0.010	ns
RE-G/RE+G	0.011	ns	0.019	ns	0.005	ns	0.009	ns	0.002	ns	0.002	ns	0.047	ns	0.007	ns
RE-O/RE+O	0.021	ns	0.024	ns	0.010	ns	0.016	ns	0.000	ns	0.002	ns	0.045	ns	0.007	ns
RE-R/RE+R	0.021	ns	0.024	ns	0.011	ns	0.016	ns	0.000	ns	0.002	ns	0.033	ns	0.005	ns
Avg(RE-/RE+)	0.019	ns	0.025	ns	0.010	ns	0.016	ns	0.000	ns	0.003	ns	0.042	ns	0.005	ns
Angle PB	0.018	ns	0.003	ns	0.014	ns	0.011	ns	0.031	ns	0.001	ns	0.038	ns	0.016	ns
Angle PG	0.017	ns	0.003	ns	0.015	ns	0.012	ns	0.026	ns	0.000	ns	0.033	ns	0.012	ns
Angle PO	0.008	ns	0.001	ns	0.010	ns	0.007	ns	0.013	ns	0.000	ns	0.031	ns	0.010	ns
Sum(P angles)	0.015	ns	0.002	ns	0.014	ns	0.010	ns	0.024	ns	0.000	ns	0.035	ns	0.013	ns
Angle RER	0.001	ns	0.001	ns	0.003	ns	0.001	ns	0.006	ns	0.001	ns	0.030	ns	0.005	ns
Angle REO	0.004	ns	0.000	ns	0.006	ns	0.003	ns	0.010	ns	0.000	ns	0.036	ns	0.008	ns
Angle REG	0.011	ns	0.001	ns	0.011	ns	0.007	ns	0.022	ns	0.000	ns	0.037	ns	0.010	ns
Sum(RE angles)	0.004	ns	0.000	ns	0.006	ns	0.003	ns	0.011	ns	0.000	ns	0.034	ns	0.007	ns

Table 6: The relationship of different reflectance band combinations on belowground stored carbon in the lower sediment layer (20-30 cm).
p ≤ 0.051 – 0.06 . *p ≤ 0.05 = ** *p ≤ 0.01 = *** *p ≤ 0 .001 = **** *p < 0.0001 = *****

Predictor	20-30 cm															
	All data								Gaps excluded							
	Mass LOI (%)		Organic C		Inorganic C		Total C		Mass LOI (%)		Organic C		Inorganic C		Total C	
	R^2	P	R^2	P	R^2	P	R^2	P	R^2	P	R^2	P	R^2	P	R^2	P
Purple	0.072	ns	0.014	ns	0.038	ns	0.003	ns	0.077	ns	0.036	ns	0.044	ns	0.009	ns
Blue	0.071	ns	0.007	ns	0.036	ns	0.005	ns	0.079	ns	0.016	ns	0.055	ns	0.000	ns
Green	0.065	ns	0.006	ns	0.038	ns	0.007	ns	0.075	ns	0.010	ns	0.057	ns	0.000	ns
Orange	0.049	ns	0.005	ns	0.032	ns	0.006	ns	0.059	ns	0.007	ns	0.052	ns	0.001	ns
Red	0.050	ns	0.005	ns	0.033	ns	0.006	ns	0.059	ns	0.008	ns	0.054	ns	0.000	ns
Red Edge	0.043	ns	0.003	ns	0.038	ns	0.010	ns	0.050	ns	0.006	ns	0.011	ns	0.001	ns
NIR	0.063	ns	0.007	ns	0.050	ns	0.011	ns	0.061	ns	0.021	ns	0.024	ns	0.006	ns
B:P	0.031	ns	0.002	ns	0.016	ns	0.003	ns	0.042	ns	0.001	ns	0.041	ns	0.003	ns
G:P	0.025	ns	0.003	ns	0.022	ns	0.005	ns	0.040	ns	0.001	ns	0.059	ns	0.006	ns
O:P	0.006	ns	0.003	ns	0.011	ns	0.001	ns	0.015	ns	0.000	ns	0.045	ns	0.012	ns
R:P	0.006	ns	0.002	ns	0.014	ns	0.003	ns	0.014	ns	0.000	ns	0.043	ns	0.012	ns
RE:P	0.001	ns	0.012	ns	0.002	ns	0.014	ns	0.002	ns	0.047	ns	0.075	ns	0.009	ns
Avg(P ratios)	0.014	ns	0.002	ns	0.018	ns	0.005	ns	0.026	ns	0.000	ns	0.038	ns	0.010	ns
P:RE	0.012	ns	0.007	ns	0.000	ns	0.005	ns	0.014	ns	0.045	ns	0.064	ns	0.010	ns
B:RE	0.040	ns	0.006	ns	0.009	ns	0.000	ns	0.051	ns	0.022	ns	0.103	ns	0.000	ns
G:RE	0.036	ns	0.005	ns	0.016	ns	0.001	ns	0.051	ns	0.014	ns	0.110	.	0.001	ns
O:RE	0.017	ns	0.007	ns	0.008	ns	0.000	ns	0.029	ns	0.010	ns	0.109	.	0.003	ns
R:RE	0.018	ns	0.006	ns	0.010	ns	0.000	ns	0.030	ns	0.013	ns	0.130	.	0.003	ns
Avg(RE ratios)	0.027	ns	0.006	ns	0.010	ns	0.000	ns	0.040	ns	0.017	ns	0.113	.	0.001	ns
1/G	0.028	ns	0.019	ns	0.020	ns	0.000	ns	0.039	ns	0.029	ns	0.093	ns	0.001	ns
1/B:P	0.019	ns	0.010	ns	0.012	ns	0.000	ns	0.031	ns	0.011	ns	0.099	ns	0.002	ns
1/B:RE	0.010	ns	0.019	ns	0.001	ns	0.008	ns	0.017	ns	0.046	ns	0.124	.	0.003	ns
1/R:RE	0.001	ns	0.019	ns	0.001	ns	0.008	ns	0.005	ns	0.033	ns	0.143	.	0.000	ns
1/Avg(P ratios)	0.006	ns	0.008	ns	0.014	ns	0.000	ns	0.016	ns	0.003	ns	0.094	ns	0.008	ns
1/Avg(RE ratios)	0.004	ns	0.020	ns	0.001	ns	0.008	ns	0.011	ns	0.040	ns	0.133	.	0.001	ns
NDVI	0.027	ns	0.015	ns	0.014	ns	0.034	ns	0.014	ns	0.006	ns	0.120	.	0.007	ns
NIR-RE/NIR+RE	0.005	ns	0.015	ns	0.003	ns	0.003	ns	0.012	ns	0.026	ns	0.141	.	0.000	ns
P-B/P+B	0.025	ns	0.006	ns	0.015	ns	0.001	ns	0.037	ns	0.007	ns	0.078	ns	0.002	ns
P-G/P+G	0.016	ns	0.010	ns	0.017	ns	0.000	ns	0.030	ns	0.010	ns	0.095	ns	0.002	ns
P-O/P+O	0.001	ns	0.008	ns	0.008	ns	0.000	ns	0.007	ns	0.002	ns	0.081	ns	0.009	ns
P-R/P+R	0.002	ns	0.006	ns	0.011	ns	0.000	ns	0.008	ns	0.001	ns	0.083	ns	0.012	ns
P-RE/P+RE	0.005	ns	0.010	ns	0.001	ns	0.011	ns	0.006	ns	0.052	ns	0.070	ns	0.012	ns
Avg(P-/P+)	0.006	ns	0.005	ns	0.015	ns	0.001	ns	0.015	ns	0.000	ns	0.062	ns	0.009	ns
RE-P/RE+P	0.005	ns	0.010	ns	0.001	ns	0.011	ns	0.006	ns	0.052	ns	0.070	ns	0.012	ns
RE-B/RE+B	0.019	ns	0.014	ns	0.003	ns	0.003	ns	0.028	ns	0.037	ns	0.117	.	0.001	ns
RE-G/RE+G	0.013	ns	0.018	ns	0.005	ns	0.003	ns	0.024	ns	0.038	ns	0.128	.	0.001	ns
RE-O/RE+O	0.003	ns	0.016	ns	0.001	ns	0.005	ns	0.009	ns	0.025	ns	0.125	.	0.000	ns
RE-R/RE+R	0.005	ns	0.015	ns	0.003	ns	0.003	ns	0.012	ns	0.026	ns	0.141	.	0.000	ns
Avg(RE-/RE+)	0.009	ns	0.016	ns	0.002	ns	0.005	ns	0.017	ns	0.037	ns	0.130	.	0.001	ns
Angle PB	0.062	ns	0.003	ns	0.030	ns	0.008	ns	0.073	ns	0.004	ns	0.060	ns	0.002	ns
Angle PG	0.058	ns	0.003	ns	0.035	ns	0.009	ns	0.070	ns	0.005	ns	0.061	ns	0.002	ns
Angle PO	0.036	ns	0.002	ns	0.026	ns	0.006	ns	0.047	ns	0.001	ns	0.053	ns	0.006	ns
Sum(P angles)	0.054	ns	0.003	ns	0.031	ns	0.008	ns	0.065	ns	0.003	ns	0.059	ns	0.003	ns
Angle RER	0.040	ns	0.005	ns	0.022	ns	0.003	ns	0.050	ns	0.008	ns	0.078	ns	0.002	ns
Angle REO	0.041	ns	0.005	ns	0.023	ns	0.003	ns	0.052	ns	0.007	ns	0.067	ns	0.002	ns
Angle REG	0.061	ns	0.005	ns	0.031	ns	0.005	ns	0.073	ns	0.011	ns	0.070	ns	0.000	ns
Sum(RE angles)	0.046	ns	0.005	ns	0.025	ns	0.003	ns	0.057	ns	0.008	ns	0.073	ns	0.001	ns

CHAPTER 6

DISCUSSION AND CONCLUSIONS

Hypothesis I: Seagrass cover can be predicted from multispectral reflectance values.

1.a. Vignetting, Directional Bias, and Other Variance Factors

Our initial hypothesis theorized that vignetting, directional bias, flight altitude, water depth and sediment bulk density may create noise within the data. The vignetting effect would cause quadrats farther away from the center of the image to have lower reflectance values than the same quadrats closer to the center of a different image. Because there is often no relationship, or the reflectance values are higher farther from the center, we reject our hypothesis that the vignetting effect would be present in the images.

Another possible source of image noise was the angle of solar radiation entry that would cause a directional bias in the reflectance values for a given quadrat. As the sunlight was entering the water from the southeast at the time of both flights, we expected that quadrats in the southeast corner of the images would have lower reflectance across wavelengths than the same quadrats in different sections of other images. We found that some cardinal directions have higher reflectance values than others and which directions have the highest reflectance differs between days and across individual images. This cannot be attributed to interference from solar angle. However, these directional biases are consistent across wavelengths, and using ratios of

the bands to each other rather than single bands helps rectify this issue.

Reflectance values did vary based on date, depth, altitude, and sediment bulk density. The amount of variance is not consistent across different cover categories. In some cases, as in the case of variance by flight day, these factors have non-additive interactions and are difficult to separate from each other. For example, the second day of imagery was in a different season, at a different altitude, and imaged a particular cover category in an area that was typically deeper and had higher bulk density. For example, soil bulk density was a more influential factor on the purple and red-edge bands on the second flight day than the first, but this is likely due to the fact that the spread of bulk density values was greater on the second day (0.3774 – 1.1308 g/cm^3) than on the first (0.1444 – 0.5529 g/cm^3). Date, altitude, depth, and bulk density are confounded with each other, and with other predictors like seagrass cover category (Fig. 9). Some of the variance in reflectance is likely due to factors like altitude or water depth, but the effects of these factors cannot be reliably isolated from the variance resulting from actual differences in seagrass cover. One solution is to use ratios of reflectance values, which are not as subject to variation arising from these abiotic

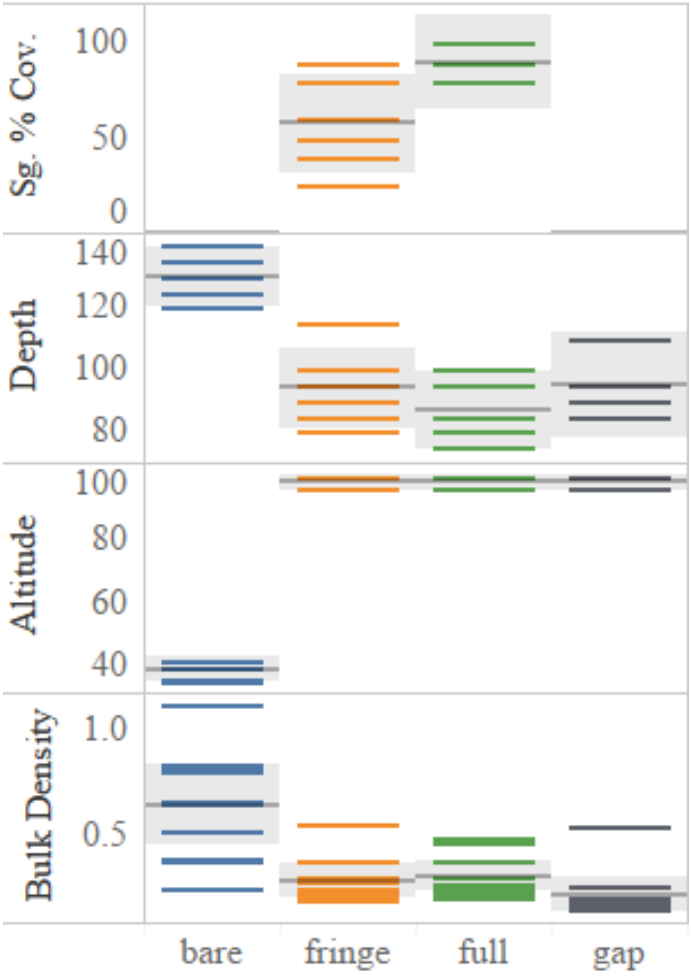

Figure 9: Confounding factors by seagrass cover category.

confounding factors as are individual reflectance values. One possible solution to these issues is to use reflectance ratios, which are not as subject to variation arising from being measured on different days or at different altitudes. This is not a perfect solution, however, because some wavelengths are influenced more or differently by certain factors than others. For example, red wavelengths are more influenced by water depth than blue, so using ratios does not entirely rectify this problem.

1.b. Ratios versus Single Band Models

As we hypothesized, ratios of bands to each other were better predictors of reflectance than single band reflectance alone, although single bands were more useful than expected. The inverse of the green band (1/G) was a particularly good predictor of seagrass cover ($p < 0.0001$, $R^2 = 0.515 – 0.567$). Furthermore, some ratios and other calculations, including spectral angle calculations, are not particularly good indicators of seagrass cover.

1.c. Single versus Multi-image Models

In many cases, single image reflectance values explained about as much or more variance in seagrass cover than when using four reflectance values as separate data points. Single image reflectance metrics produced similarly significant models for predicting seagrass cover as multiple images. In some instances, multiple images were better, in other cases, single images were better or produced similar significance. However, the average values for different reflection metrics derived from multiple images were nearly always better predictors than either the single image values or the four values considered as separate data points (Fig. 10).

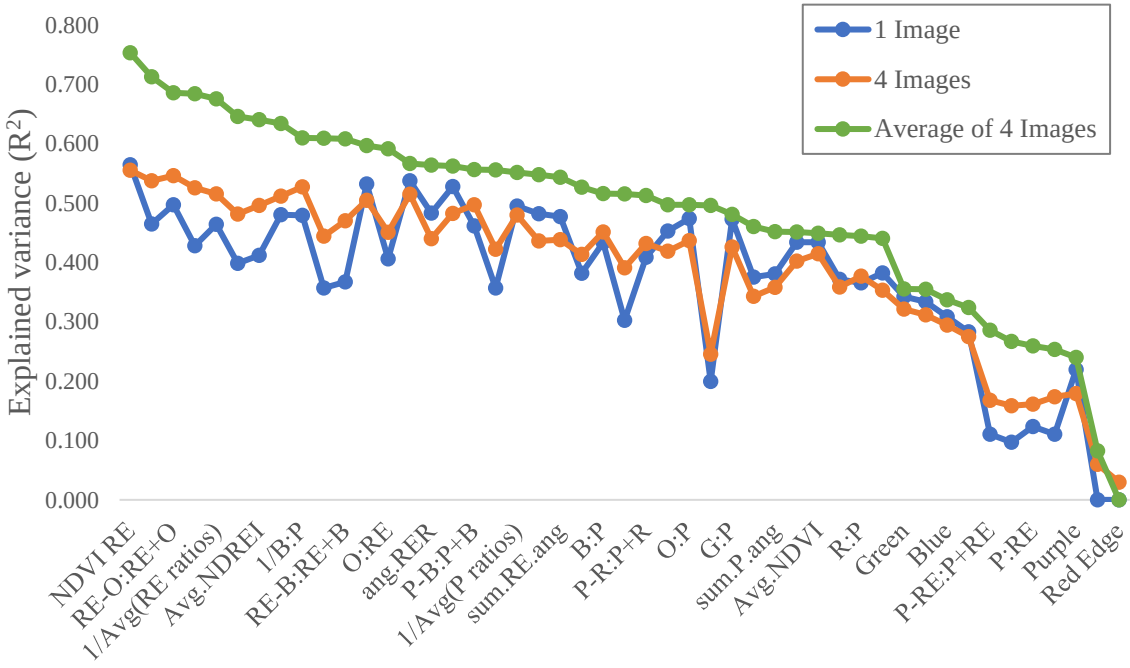

Figure 10: Amount of variance (R^2) in various reflectance models explained by a single image, 4 images, and the multi-image averages.

1.d. NDVI as a Predictor of Seagrass Cover

NDVI, calculated as (NIR − Red) / (NIR + Red), was not useful when considering single images (R^2 = 0.200) or multiple images as separate data points (R^2 = 0.245), but it was a reasonably good predictor when considering its average across multiple images (R^2 = 0.556). Furthermore, the best predictor of seagrass cover that we found was a variation of NDVI, which we calculated as (NIR − Red Edge) / (NIR + Red Edge). Red-edge falls just between red and NIR on the spectrum.

The reliability of metrics that use red-edge and/or NIR is questionable in deeper waters. Our sample area was shallow (<1.5 m) with generally clear water, so attenuation of red and IR wavelengths was less than would be expected in many other areas where seagrass grows. Our images still showed some detail in NIR, although NIR was less detailed than the shorter

wavelengths (Fig. 13). We expect that the reliability of any predictor that include NIR or red edge wavelengths will decrease as the depth of the water being surveyed increases. A similar study using multispectral imagery to predict seagrass cover found a similar NIR in dense seagrass cover but excluded NIR from consideration due to light scattering (Schweizer et al., 2005). Previous studies have created models that account for NIR reflectance in waters that NIR scattering may not be as prevalent, although further study of our site would be needed to accurately create a model that accounted for this (Bailey et al., 2010).

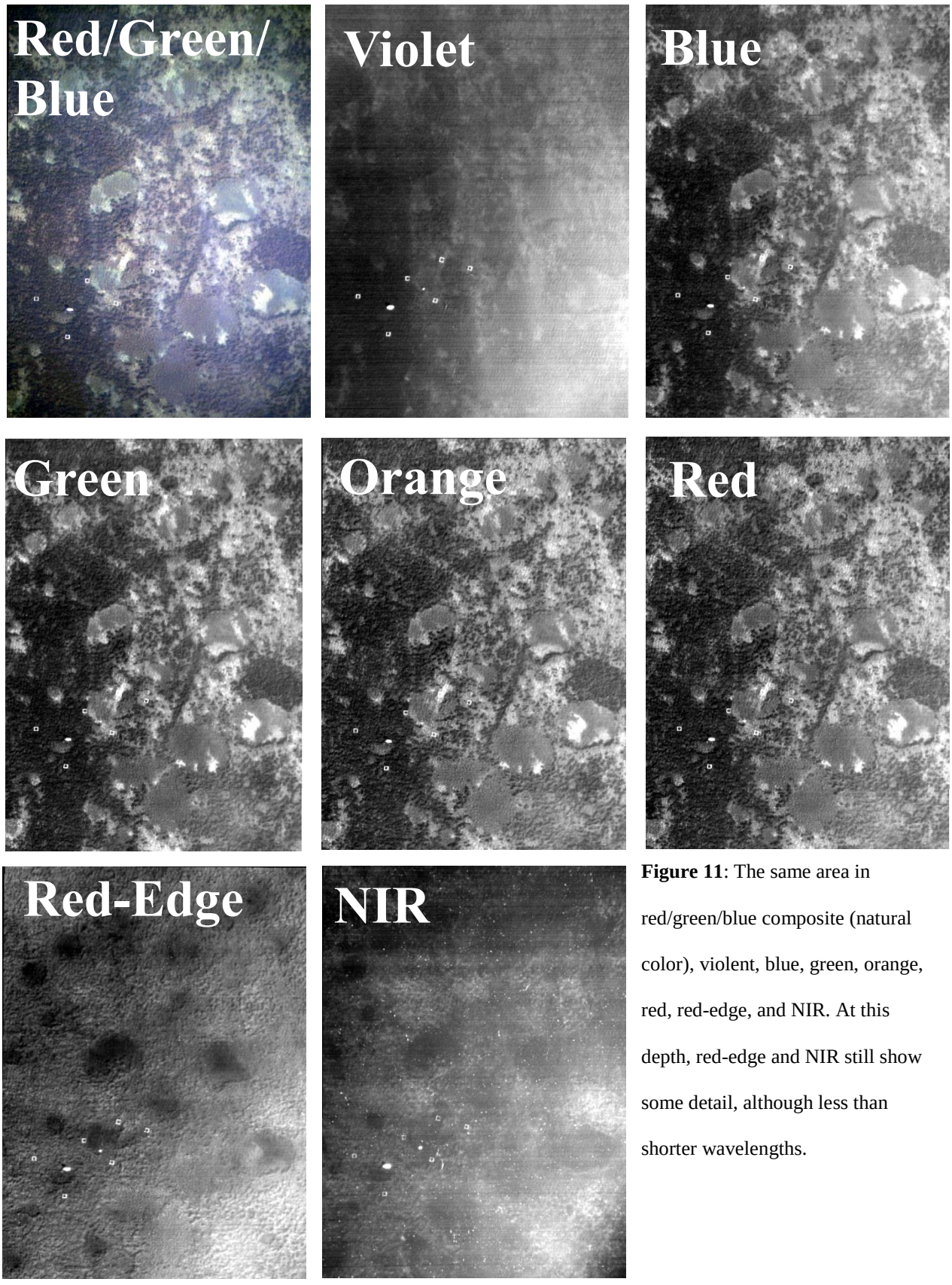

Figure 11: The same area in red/green/blue composite (natural color), violent, blue, green, orange, red, red-edge, and NIR. At this depth, red-edge and NIR still show some detail, although less than shorter wavelengths.

Summary

Applying this research on a larger scale may introduce new challenges. UAVs are sensitive to weather conditions, such as wind and rain and, and while UAV surveys can produce very fine-scale spatial resolution, mounting a multispectral sensor onto a low-flying aircraft may be more appropriate for annual mapping. Applications of UAVs could provide low cost solutions for small management organizations that only wish to create baseline surveys. UAVs also could be especially useful in monitoring small areas affected by human activity, such as construction projects.

Our results suggest that predicting seagrass cover from multispectral reflectance values is possible. Accounting for factors that influence reflectance outside of seagrass cover can improve predictions. Averaging reflectance values across multiple images and using band ratios and indices instead of single bands also improves the fit of prediction models. At shallow depths, red, red-edge, and NIR prove useful in predicting seagrass cover (Table 7). When excluding models that use red, red-edge, or NIR metrics, the ratio of blue to purple model explains variance well ($R^2 = 0.610$). If only red, green, and blue wavelengths are available (as is the case with a standard camera), the inverse ratio of green can be useful in predicting seagrass cover.

Table 7: Ranking of reflectance metrics' goodness-of-fit (R^2) and significance (p), listed in descending order of based on the amount of variance explained by the four-image average.
$p \leq 0.051 – 0.06$. $p \leq 0.05$ = * $p \leq 0.01$ = ** $p \leq 0.001$ = *** $p < 0.0001$ = ****

Predictor					Average of 4 Images		
					R^2	P	Rank
Ratio	Near IR	- Red Edge	/ Near IR	+ Red Edge	0.753	****	1
Inverse ratio	Red		Red Edge		0.713	****	2
Ratio	Red Edge	- Orange	/ Red Edge	+ Orange	0.686	****	3
Ratio	Red Edge	- Red	/ Red Edge	+ Red	0.684	****	4
Inverse Average	Ratios		Red Edge		0.676	****	5
Inverse ratio	Blue		Red Edge		0.646	****	6
Average	Ratios		**Above P B G O R -/+ RE Palues**		0.641	****	7
Ratio	Red Edge	- Green	/ Red Edge	+ Green	0.634	****	8
Inverse ratio	Blue		Purple		0.610	****	9
Ratio	Red		Red Edge		0.609	****	10
Ratio	Red Edge	- Blue	/ Red Edge	+ Blue	0.608	****	11
Ratio	Purple	- Orange	/ Purple	+ Orange	0.597	****	12
Ratio	Orange		Red Edge		0.592	****	13
Inverse band	Green				0.567	****	14
Angle	Red Edge		Red		0.564	****	15
Ratio	Purple	- Green	/ Purple	+ Green	0.562	****	16
Ratio	Purple	- Blue	/ Purple	+ Blue	0.556	****	17
Average	Ratios		Red Edge		0.556	****	18
Inverse Average	Ratios		Purple		0.551	****	19
Angle	Red Edge		Orange		0.548	****	20
Sum	Angles		Red Edge		0.543	****	21
Ratio	Green		Red Edge		0.527	****	22
Ratio	Blue		Purple		0.516	****	23
Ratio	Blue		Red Edge		0.515	***	24
Ratio	Purple	- Red	/ Purple	+ Red	0.513	****	25
Angle	Red Edge		Green		0.497	****	26
Ratio	Orange		Purple		0.497	****	27
NDVI (Ratio)	Near IR	- Red	/ Near IR	+ Red	0.496	****	28
Ratio	Green		Purple		0.481	****	29
Angle	Purple		Orange		0.461	****	30
Sum	Angles		Purple		0.452	****	31
Average	Ratios		Purple		0.451	****	32
Average	Ratios		**Above B G O R RE -/+ P Palues**		0.449	****	33
Angle	Purple		Blue		0.447	****	34
Ratio	Red		Purple		0.444	****	35
Angle	Purple		Green		0.441	****	36
Single band	Green				0.356	****	37
Single band	Orange				0.355	***	38
Single band	Blue				0.337	***	39
Single band	Red				0.324	***	40
Ratio	Purple	- Red Edge	/ Purple	+ Red Edge	0.286	***	41
Ratio	Red Edge		Purple		0.267	**	42
Ratio	Purple		Red Edge		0.260	Ns	43
Ratio	Red Edge	- Purple	/ Red Edge	+ Purple	0.253	****	44
Single band	Purple				0.240	**	45
Single band	Near IR				0.082	.	46
Single band	Red Edge				0.000	Ns	47

Hypothesis II: Seagrass cover predicts belowground carbon storage.

Mind the Gap. The significant linear relationships observed between seagrass cover and organic carbon (via mass LOI), inorganic carbon, and total carbon (as measured via an elemental analyzer) for the 10-20 cm layer when considering all samples, including gaps, are negative. A negative relationship is contrary to expectations and to our understanding of seagrass ecology and biogeochemistry. These patterns are driven by the inclusion of seagrass bed gaps, which have zero seagrass cover but enriched sedimentary carbon, even relative to dense seagrass beds nearby, and dominate the relatively subtle relationships between seagrass cover and sedimentary carbon.

Although these gaps, often termed underwater fairy circles, are a documented phenomenon, there is little agreement in the scientific community as to why they form. Considering gaps were found to at greater depths than the surrounding and that the upper layer of sediment was of a lower bulk density, we theorized that these patches are areas of recent seagrass loss. This may help explain why carbon stocks were higher in these areas than the surrounding areas, as the decomposition of seagrass biomass that had previously occupied the area would contribute to sedimentary carbon. Studies of underwater fairy circles in Mediterranean eelgrass beds (*Zostera marina*) supported the theory that these are areas of seagrass death due to competition, i.e. seagrass shoot density becomes so great in these areas that seagrass dies out from the center (Ruiz-Reynés et al., 2017). This also explains why the fringe seagrass category generally had higher organic carbon content than the surrounding seagrass beds, as shoot density is highest surrounding these circles and therefore may trap more particulate organic matter

(POM), as well as deposit more plant matter (Ruiz-Reynés et al., 2017). Another study on *Z. marina* found that nutrient limitation is the driving factor in fairy circle formation (Borum et al., 2014). Another possible explanation would be the oscillation of water currents in these deeper, circular patches that could cause POM. An isotopic analysis of sedimentary carbon in the area could help explain the origin of the gaps often found in seagrass cover.

Carbon Storage Estimates Excluding Gaps. Excluding the gap category improved our prediction models in the top layer of sediment. Organic carbon (via mass LOI), inorganic carbon, and total carbon all showed a positive relationship with seagrass cover, although these relationships were weaker than expected (Fig. 12). As expected, organic carbon also decreased with depth in the sediment layer (Fig 13).

The dynamic nature of seagrass bed patterns may help explain why the relationships between aboveground cover and belowground stored carbon is weaker in our study area than would be expected in a terrestrial ecosystem. A study on *Z. marina* found than in the 7 years between mapping efforts, 39-62% of seagrass cover had changed (either died off or made a comeback) (Frederiksen et al., 2004). This further highlights the need for frequent assessments.

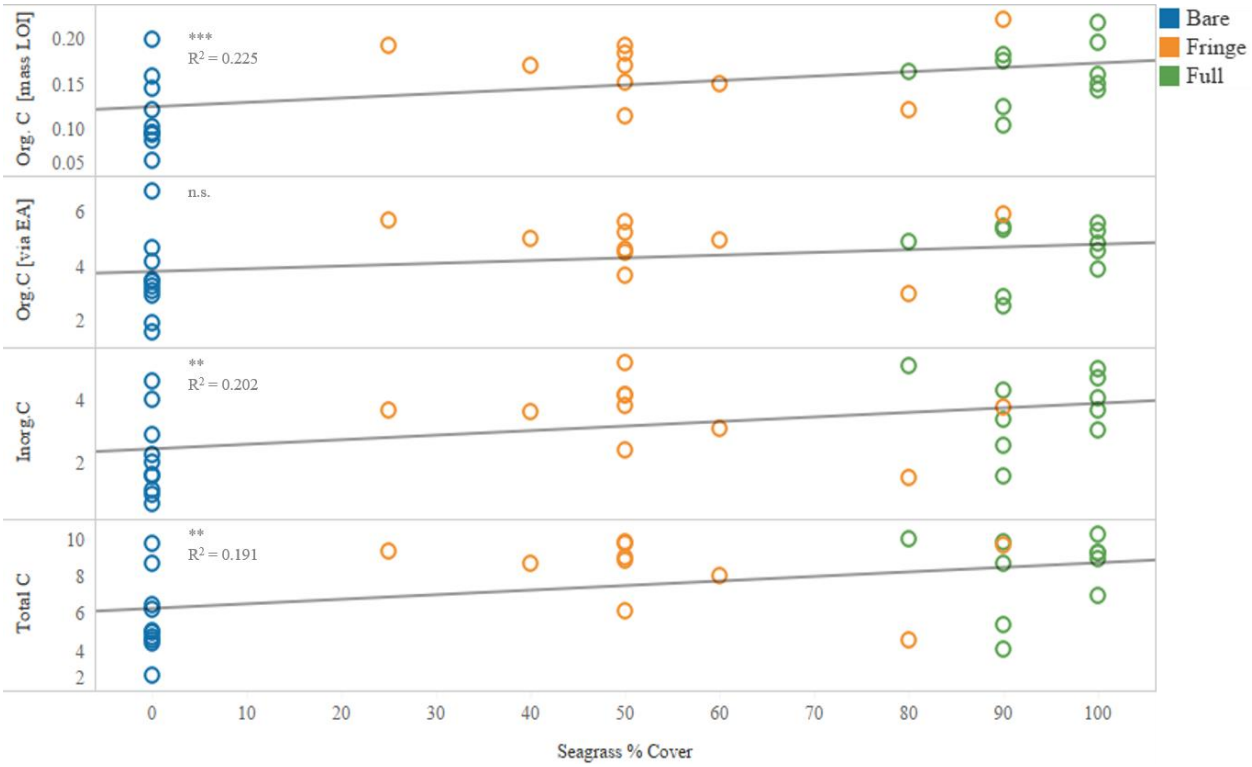

Figure 12: The linear relationships between seagrass cover and percent (%) total carbon, inorganic carbon, and organic carbon, when excluding seagrass gaps in the topmost layer of sediment (0-10 cm).
p ≤ 0.051 – 0.06 . *p ≤ 0.05* = * *p ≤ 0.01* = ** *p ≤ 0 .001* = *** *p < 0.0001* = ****

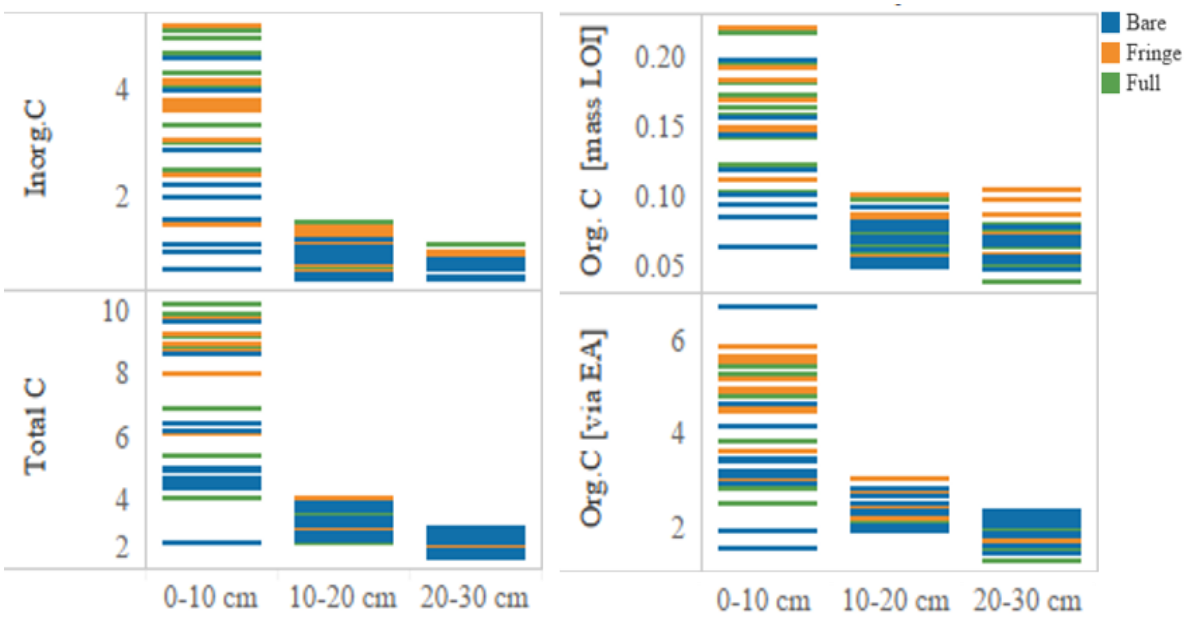

Figure 13: Percent (%) sedimentary total, inorganic, and organic carbon decreases with depth and the top 10 cm of sediment has the most variability in the amount of belowground stored carbon.

Hypothesis III: Multispectral reflectance can be used to estimate sedimentary carbon.

Recently, advances in making Sedimentary carbon estimates from remotely sensed data have emerged. Generally, these studies have worked with terrestrial systems. Chen et al. (2019) found that reflectance was a key component in determining soil organic matter (SOM) in croplands. NIR, red, blue, and green bands were all used to generate soil models, though additional environmental factors such as soil moisture content were also used in the models. A similar study found that NDVI, when used in conjunction with field measurements, could help provide litter and Sedimentary carbon estimates for forested areas (Cao et al., 2019).

As using reflectance to create models that predict belowground stored carbon in terrestrial ecosystems is a fairly new approach, few instances of these types of models exist for use in underwater systems. Our attempts to generate these models showed some promise, though only in the topmost (0-10 cm) layer of sediment. Models generated for this layer (and excluding the gap category) in our study have shown that reflectance can be a reasonably good indicator of belowground stored carbon, with some relationship showing high significance ($p < 0.0001$) and R^2 values as high as 0.475 (Table 8). Different ratios of green and red-edge and the inverse of green reflectance produced the most significant models across all carbon categories, although metrics using red, red-edge, and NIR could be less useful in deeper water. Purple, blue, and green reflectance, which would not dissipate as readily in deeper water, also showed promise in predicting organic carbon storage.

Table 8: A ranking of the relationship between various reflectance predictors and sedimentary carbon for the top layer (0-10 cm) of sediment, when the gap cover category is excluded.
$p \leq 0.051 – 0.06$. $p \leq 0.05$ = * $p \leq 0.01$ = ** $p \leq 0.001$ = *** $p < 0.0001$ = ****

0-10 cm depth, gaps excluded												
Rank	Organic C (%, via LOI)			Organic C (%, via EA)			Inorganic C (%, via EA)			Total C (%, via EA)		
	Predictor	R^2	P	Predictor	R^2	P	Predictor	R^2	P	Predictor	R^2	P
1	G:RE	0.466	****	1/G	0.409	***	G:RE	0.457	***	G:RE	0.475	****
2	1/G	0.445	***	Purple	0.396	***	B:RE	0.441	***	Avg(RE ratios)	0.446	***
3	Avg(RE ratios)	0.441	***	Blue	0.392	***	Avg(RE ratios)	0.434	***	O:RE	0.441	***
4	B:RE	0.441	***	Green	0.390	***	RE-B/RE+B	0.422	***	B:RE	0.439	***
5	O:RE	0.434	***	Angle REG	0.382	***	O:RE	0.421	***	RE-G/RE+G	0.436	***
6	R:RE	0.425	***	Angle PG	0.369	***	RE-G/RE+G	0.410	***	R:RE	0.428	***
7	RE-G/RE+G	0.422	***	Orange	0.366	***	1/B:RE	0.400	***	RE-B/RE+B	0.424	***
8	RE-B/RE+B	0.420	***	Sum(RE angles)	0.361	***	Avg(RE-/RE+)	0.391	***	Angle REG	0.420	***
9	Angle REG	0.416	***	Red	0.360	***	R:RE	0.390	***	Avg(RE-/RE+)	0.405	***
10	Avg(RE-/RE+)	0.397	***	Angle REO	0.355	**	1/Avg(RE ratios)	0.372	***	1/B:RE	0.405	***
11	1/B:RE	0.396	***	Sum(P angles)	0.354	**	RE-O/RE+O	0.369	***	1/G	0.402	***
12	1/B:P	0.391	***	Angle PB	0.350	**	NIR-RE/NIR+RE	0.345	**	P-G/P+G	0.399	***
13	P-B/P+B	0.390	***	NIR	0.348	**	RE-R/RE+R	0.345	**	1/B:P	0.396	***
14	P-G/P+G	0.386	***	Angle RER	0.348	**	P-B/P+B	0.333	**	RE-O/RE+O	0.394	***
15	RE-O/RE+O	0.386	***	Angle PO	0.327	**	1/B:P	0.332	**	1/Avg(RE ratios)	0.391	***
16	Sum(RE angles)	0.384	***	P-G/P+G	0.315	**	G:P	0.332	**	P-B/P+B	0.391	***
17	NIR-RE/NIR+RE	0.384	***	G:RE	0.314	**	P-G/P+G	0.329	**	Sum(RE angles)	0.389	***
18	RE-R/RE+R	0.384	***	1/B:P	0.307	**	1/R:RE	0.313	**	NIR-RE/NIR+RE	0.387	***
19	1/Avg(RE ratios)	0.381	***	R:RE	0.301	**	B:P	0.306	**	RE-R/RE+R	0.387	***
20	Angle REO	0.377	***	P-B/P+B	0.297	**	Angle REG	0.302	**	G:P	0.383	***
21	G:P	0.376	***	RE-G/RE+G	0.296	**	Sum(RE angles)	0.273	**	Angle PB	0.382	***
22	Angle PB	0.376	***	O:RE	0.294	**	Angle PB	0.273	**	Angle PG	0.381	***
23	Angle PG	0.372	***	Avg(RE ratios)	0.289	**	Angle REO	0.266	**	Angle REO	0.380	***
24	Green	0.371	***	G:P	0.286	**	Angle RER	0.257	**	Angle RER	0.370	***
25	Blue	0.368	***	1/Avg(P ratios)	0.283	**	Angle PG	0.256	**	Sum(P angles)	0.369	***
26	Angle RER	0.365	***	NIR-RE/NIR+RE	0.280	**	1/G	0.255	**	Green	0.367	***
27	Sum(P angles)	0.361	***	RE-R/RE+R	0.280	**	1/Avg(P ratios)	0.250	**	1/R:RE	0.356	**
28	1/R:RE	0.353	**	B:RE	0.274	**	Sum(P angles)	0.250	**	Blue	0.353	**
29	B:P	0.350	**	RE-O/RE+O	0.270	**	P-O/P+O	0.248	**	B:P	0.340	**
30	Orange	0.330	**	RE-B/RE+B	0.268	**	O:P	0.246	**	1/Avg(P ratios)	0.329	**
31	1/Avg(P ratios)	0.322	**	Avg(RE-/RE+)	0.265	**	P:RE	0.238	**	Orange	0.324	**
32	Purple	0.318	**	1/Avg(RE ratios)	0.262	**	Avg(P ratios)	0.235	*	Angle PO	0.321	**
33	Angle PO	0.312	**	P-O/P+O	0.262	**	Green	0.220	*	P-O/P+O	0.315	**
34	P-O/P+O	0.309	**	1/R:RE	0.262	**	Angle PO	0.203	*	Red	0.296	**
35	Red	0.304	**	1/B:RE	0.258	**	P-RE/P+RE	0.201	*	O:P	0.296	**
36	O:P	0.294	**	Red Edge	0.255	**	RE-P/RE+P	0.201	*	Avg(P ratios)	0.285	**
37	Avg(P ratios)	0.287	**	Avg(P-/P+)	0.243	**	Blue	0.200	*	Purple	0.282	**
38	Avg(P-/P+)	0.269	**	B:P	0.243	**	Avg(P-/P+)	0.200	*	Avg(P-/P+)	0.272	**
39	P-R/P+R	0.258	**	P-R/P+R	0.241	**	Orange	0.180	*	P-R/P+R	0.258	**
40	R:P	0.234	*	O:P	0.231	*	P-R/P+R	0.180	*	R:P	0.230	*
41	NIR	0.192	*	Avg(P ratios)	0.225	*	R:P	0.172	*	P:RE	0.186	*
42	P:RE	0.189	*	R:P	0.201	*	NDVI	0.161	*	NIR	0.181	*
43	P-RE/P+RE	0.154	*	P:RE	0.079	ns	Red	0.148	*	P-RE/P+RE	0.158	*
44	RE-P/RE+P	0.154	*	P-RE/P+RE	0.068	ns	RE:P	0.131	.	RE-P/RE+P	0.158	*
45	Red Edge	0.124	.	RE-P/RE+P	0.068	ns	Purple	0.112	.	RE:P	0.113	.
46	RE:P	0.101	ns	RE:P	0.057	ns	NIR	0.035	ns	Red Edge	0.106	.
47	NDVI	0.059	ns	NDVI	0.006	ns	Red Edge	0.009	ns	NDVI	0.074	ns

Limitations to Using Reflectance to Predict Carbon Storage

Carbon Storage Varies by Species and the Surrounding Ecosystem. Previous studies have documented the variability of carbon storage in seagrass beds across both large and small spatial scales. Different seagrass species have different carbon storage rates and generally larger species have a greater storage potential than smaller species (Lavery et al., 2013). Mixed species beds may also store carbon differently than single species beds. Productivity, which is dependent on short-term nutrient availability, and long-term nutrient history both affect carbon storage rates (Lavery et al., 2013, Armitage and Fourqurean, 2016).

Since as much as 50% of carbon stored within seagrass beds comes from allochthonous sources, the larger landscape surrounding seagrass beds and well as prevailing currents in the areas could also influence carbon deposition (Kennedy et al., 2010). Additionally, other abiotic factors such as water depth affect carbon storage potential of seagrass beds (Serrano et al., 2014). The best solution for accounting for these factors is to establish baselines for each species within a large area and then use reflectance data to extrapolate the carbon storage potential of a larger area.

Gaps. As gaps contain higher belowground stored carbon than the surrounding seagrass beds and much higher carbon than bare patches, while producing similar reflectance to bare patches, making carbon estimates without accounting for these anomalies may produce inaccurate estimations. To remedy this, gaps should be included in establishing a baseline carbon storage for an area. Questions as to whether this carbon should be considered as stored also arise and depend on the origin (and therefore long-term storage potential) of the carbon. If the carbon

came from outside sources, will the bare area be able to bury that carbon as well as areas of dense seagrass? If the carbon came from locally decomposing seagrass, do these bare patches represent a release of carbon back into the atmosphere or do the surrounding seagrass beds aid in recapturing the suspending organic matter? Gaps within the seagrass matrix present an interesting case for future study.

Reflectance May Vary by Season. Senescence, or the seasonal yellowing of leaves, can present an issue for vegetation mapping. Some seagrasses also experience this yearly die-off. Since this causes a change in the amount of chlorophyll in the leaf tissue, the wavelengths that the leaves reflect also change (Fig. 14). To prevent this issue, reflectance values should be gathered at approximately the same time each year, especially in more temperate areas.

.

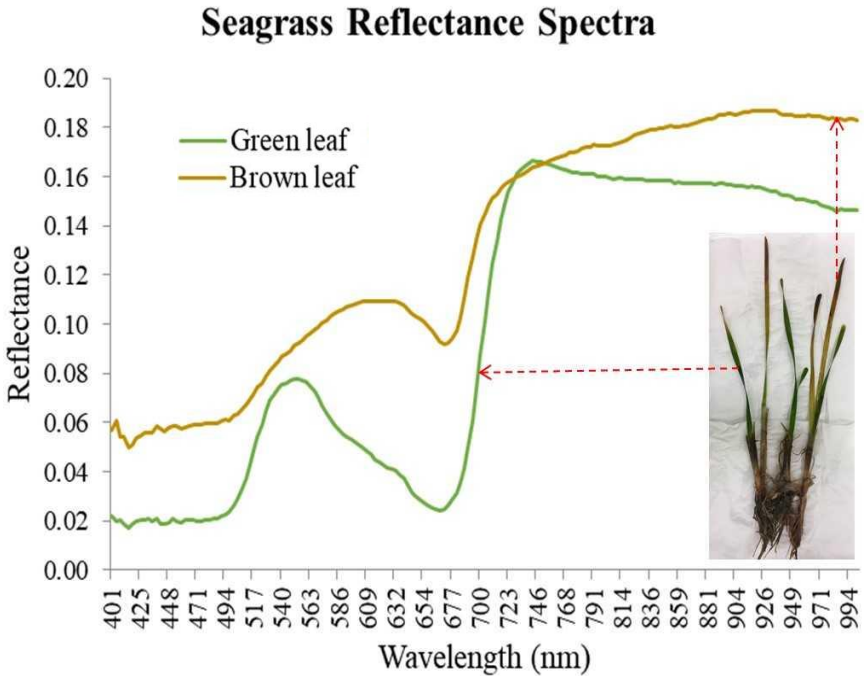

Figure 14: Difference in reflectance values of green and brown blades of T. testudinum.

Conclusions

Seagrass maps that rely on point data can be both time consuming and over- or underestimate total coverage. One model suggests that seagrass beds may occupy more than twice the current estimates from traditional mapping techniques (Jayathilake and Costello, 2018). Methods for estimating seagrass coverage are essential for planning and management. Remote sensing using multispectral sensors may provide a better methodology. Our use of drones to measure spectral reflectance to estimate seagrass cover can be used to generate maps that have fine spatial (give resolution) and temporal scales and are less time and labor intensive. This technique can be scaled up for larger areas or used with UAVs to achieve fine-scale resolution.

Terrestrial belowground carbon storage has been found to coincide with aboveground vegetation density (Ryan, 1991). This link is suspected but not well studied in aquatic ecosystems. This research has shown that seagrass coverage relates to belowground carbon storage, within the upper soil profile. Establishing this relationship has implications for how carbon storage is estimated within seagrass meadows. Previous studies have concluded that organic carbon storage is influenced by many factors, including abiotic and biotic variables, so baselines for different geographic areas need to be further explored (Samper-Villarreal, 2016). Since seagrasses are one of the largest carbon sinks worldwide, being able to easily map and from these maps accurately predict carbon storage will have implications for protecting seagrass habitat and for scientists attempting to mitigate the effects of climate change.

REFERENCES

Armitage, A. R., & Fourqurean, J. W. (2016). Carbon storage in seagrass soils: long-term nutrient history exceeds the effects of near-term nutrient enrichment.

Bailey, S. W., Franz, B. A., & Werdell, P. J. (2010). Estimation of near-infrared water-leaving reflectance for satellite ocean color data processing. *Optics express*, *18*(7), 7521-7527.

Borsje, B. W., van Wesenbeeck, B. K., Dekker, F., Paalvast, P., Bouma, T. J., van Katwijk, M. M., & de Vries, M. B. (2011). How ecological engineering can serve in coastal protection. *Ecological Engineering*, *37*(2), 113-122.

Borum, J., Raun, A. L., Hasler-Sheetal, H., Pedersen, M. Ø., Pedersen, O., & Holmer, M. (2014). Eelgrass fairy rings: sulfide as inhibiting agent. *Marine biology*, *161*(2), 351-358.

Calladine, A., Fourqurean, J.W., Heck Jr., K.L., Hughes, Kendrick, G. A., Kenworthy, W.J., Short, F.T., and Williams, S.L., (2009). Accelerating loss of seagrasses across the globe threatens coastal ecosystems. *Proceedings of the National Academy of Sciences*, *106*(30), 12377-12381.

Cao, B., Domke, G. M., Russell, M. B., & Walters, B. F. (2019). Spatial modeling of litter and Sedimentary carbon stocks on forest land in the conterminous United States. *Science of the Total Environment*, *654*, 94-106.

Chen, D., Chang, N., Xiao, J., Zhou, Q., & Wu, W. (2019). Mapping dynamics of soil organic matter in croplands with MODIS data and machine learning algorithms. *Science of The Total Environment*.

Christianen, M. J., van Belzen, J., Herman, P. M., van Katwijk, M. M., Lamers, L. P., van Leent, P. J., & Bouma, T. J. (2013). Low-canopy seagrass beds still provide important coastal protection services. *PloS one*, *8*(5), e62413.

Congdon, V. M., & Dunton, K. H. (2016). Tracking Long-Term Trends in Seagrass Cover and Condition in Texas Coastal Waters.

Costanza, R., d'Arge, R., De Groot, R., Farber, S., Grasso, M., Hannon, B., Limburg, K., Naeem, S., O'Neill, R.V., Paruelo, J.P., Raskin, R.G., Sutton, P., & Raskin, R. G. (1997). The value of the world's ecosystem services and natural capital. *Nature*, *387*(6630), 253-260

de la Torre-Castro, M., & Rönnbäck, P. (2004). Links between humans and seagrasses—an example from tropical East Africa. *Ocean & Coastal Management*, *47*(7), 361-387.Duarte, C. M., & Cebrian, J. (1996). The fate of marine autotrophic production. *Limnology and Oceanography*, *41*(8), 1758-1766.

Duarte, C. M., & Chiscano, C. L. (1999). Seagrass biomass and production: a reassessment. *Aquatic botany*, *65*(1), 159-174.

Fletcher, R. S., Pulich Jr, W., & Hardegree, B. (2009). A semiautomated approach for monitoring landscape changes in Texas seagrass beds from aerial photography. *Journal of coastal research*, 500-506.

Fourqurean, J. W., Duarte, C. M., Kennedy, H., Marbà, N., Holmer, M., Mateo, M. A., Apostolaki, E.T., Kendrick, G.A., Krause-Jensen, D., McGlathery, K.J., & Serrano, O. (2012). Seagrass ecosystems as a globally significant carbon stock. *Nature geoscience*, *5*(7), 505-509.

Frederiksen, M., Krause-Jensen, D., Holmer, M., & Laursen, J. S. (2004). Spatial and temporal variation in eelgrass (Zostera marina) landscapes: influence of physical setting. *Aquatic Botany*, *78*(2), 147-165.

Fry, B., & Parker, P. L. (1979). Animal diet in Texas seagrass meadows: δ13C evidence for the importance of benthic plants. *Estuarine and Coastal Marine Science*, *8*(6), 499-509.

Greene, A., Rahman, A. F., Kline, R., & Rahman, M. S. (2018). Side scan sonar: A cost-efficient alternative method for measuring seagrass cover in shallow environments. *Estuarine, Coastal and Shelf Science*, *207*, 250-2

Hemminga, M. A., & Duarte, C. M. (2000). *Seagrass ecology*. Cambridge University Press

Howard, J., Hoyt, S., Isensee, K., Telszewski, M., Pidgeon, E. (eds.)(2014). Coastal Blue Carbon: Methods for assessing carbon stocks and emissions factors in mangroves, tidal salt marshes, and seagrasses. Conservation International, Intergovernmental Oceanographic Commission of UNESCO, International Union for Conservation of Nature. Arlington, Virginia, USA.

Jayathilake, D. R., & Costello, M. J. (2018). A modelled global distribution of the seagrass biome. *Biological Conservation*, *226*, 120-126.

Kaldy, J. E., Onuf, C. P., Eldridge, P. M., & Cifuentes, L. A. (2002). Carbon budget for a subtropical seagrass dominated coastal lagoon: How important are seagrasses to total ecosystem net primary production?. *Estuaries*, *25*(4), 528-539.

Kennedy, H., Beggins, J., Duarte, C. M., Fourqurean, J. W., Holmer, M., Marbà, N., & Middelburg, J. J. (2010). Seagrass sediments as a global carbon sink: Isotopic constraints. *Global Biogeochemical Cycles*, *24*(4).

Kowalski, J. L., DeYoe, H. R., & Allison, T. C. (2009). Seasonal production and biomass of the seagrass, Halodule wrightii Aschers.(shoal grass), in a subtropical Texas lagoon. *Estuaries and coasts*, *32*(3), 467-482.

Lavery, P. S., Mateo, M. Á., Serrano, O., & Rozaimi, M. (2013). Variability in the carbon storage of seagrass habitats and its implications for global estimates of blue carbon ecosystem service. *PloS one*, *8*(9), e73748.

Mcleod, E., Chmura, G. L., Bouillon, S., Salm, R., Björk, M., Duarte, C. M., Lovelock, C.E., Schlesinger, W.H., & Silliman, B. R. (2011). A blueprint for blue carbon: toward an improved understanding of the role of vegetated coastal habitats in sequestering CO2. *Frontiers in Ecology and the Environment*, *9*(10), 552-560.

McRoy, C. P., & Helfferich, C. (1977). Seagrass ecosystems. *Marine Science (USA)*.

Myers, R. A., Baum, J. K., Shepherd, T. D., Powers, S. P., & Peterson, C. H. (2007). Cascading effects of the loss of apex predatory sharks from a coastal ocean. *Science*, *315*(5820), 1846-1850.

Onuf, C.P. 2007. Laguna Madre. In Handley, L., Altsman, D., and DeMay, R., eds., 2007, Seagrass Status and Trends in the Northern Gulf of Mexico: 1940–2002: U.S. Geological Survey Scientific Investigations Report 2006-5287, 267 p.

Orth, R. J., Carruthers, T. J., Dennison, W. C., Duarte, C. M., Fourqurean, J. W., Heck, K. L., ... & Short, F. T. (2006). A global crisis for seagrass ecosystems. *AIBS Bulletin*, *56*(12), 987-996.

Quammen, M. L., & Onuf, C. P. (1993). Laguna Madre: seagrass changes continue decades after salinity reduction. *Estuaries and coasts*, *16*(2), 302-310.

Pendleton, L., Donato, D. C., Murray, B. C., Crooks, S., Jenkins, W. A., Sifleet, S., ... & Megonigal, P. (2012). Estimating global "blue carbon" emissions from conversion and degradation of vegetated coastal ecosystems. *PloS one*, *7*(9), e43542.

Ralph, P. J., Tomasko, D., Moore, K., Seddon, S., & Macinnis-Ng, C. M. (2007). Human impacts on seagrasses: eutrophication, sedimentation, and contamination. In *SEAGRASSES: BIOLOGY, ECOLOGY AND CONSERVATION* (pp. 567-593). Springer Netherlands.

Roelfsema, C. M., Phinn, S. R., Udy, N., & Maxwell, P. (2009). An integrated field and remote sensing approach for mapping seagrass cover, Moreton Bay, Australia. *Journal of Spatial Science*, *54*(1), 45-62.

Ruiz-Reynés, D., Gomila, D., Sintes, T., Hernández-García, E., Marbà, N., & Duarte, C. M.

(2017). Fairy circle landscapes under the sea. *Science advances*, *3*(8), e1603262.

Ryan, M. G. (1991). A simple method for estimating gross carbon budgets for vegetation in forest ecosystems. *Tree physiology*, *9*(1-2), 255-266.

Samper-Villarreal, J., Lovelock, C. E., Saunders, M. I., Roelfsema, C., & Mumby, P. J. (2016). Organic carbon in seagrass sediments is influenced by seagrass canopy complexity, turbidity, wave height, and water depth. *Limnology and Oceanography*, *61*(3), 938-952.

Serrano, O., Lavery, P. S., Rozaimi, M., & Mateo, M. Á. (2014). Influence of water depth on the carbon sequestration capacity of seagrasses. *Global Biogeochemical Cycles*, 28(9), 950-961.

Armstrong, R. A. (1993). Remote sensing of submerged vegetation canopies for biomass estimation. *International Journal of Remote Sensing*, *14*(3), 621-627.

Stankovic, M., Tantipisanuh, N., & Prathep, A. (2018). Carbon storage in seagrass ecosystems along the Andaman coast of Thailand. *Botanica Marina*, 61(5), 429-440.

TDWR (Texas Department of Water Resources). 1983. *Laguna Madre Estuary: A Study of the Influence of Freshwater Inflows*. 270. Austin: Texas Department of Water Resources Report LP-182.

Van der Wal, D., & Pye, K. (2004). Patterns, rates and possible causes of saltmarsh erosion in the Greater Thames area (UK). *Geomorphology*, *61*(3), 373-391.

Waycott, M., Duarte, C. M., Carruthers, T. J., Orth, R. J., Dennison, W. C., Olyarnik, S., & Kendrick, G. A. (2009). Accelerating loss of seagrasses across the globe threatens coastal ecosystems. *Proceedings of the national academy of sciences*, *106*(30), 12377-12381.

APPENDIX A

APPENDIX A

MAIA WV MULTISPECTRAL CAMERA SPECIFICATIONS

MAIA MV 9-band multispectral camera and associated Incoming Light Sensor.

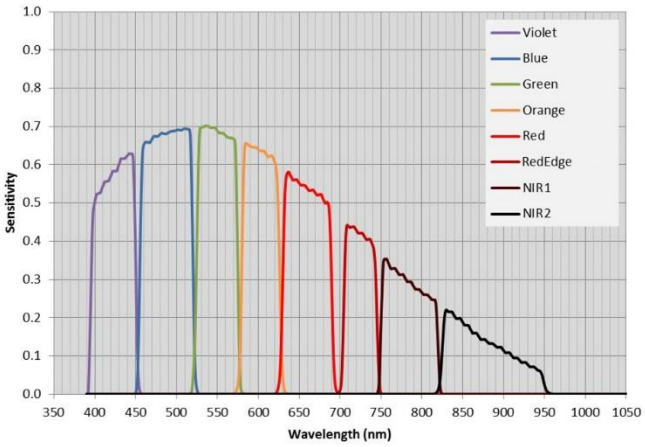

Spectral sensitivity of the MAIA MV sensor.

Sensor	Start WL(nm)	Stop WL (nm)	CWL (nm)	FWHM (nm)	Color
S1	395	450	422.5	55	PURPLE
S2	455	520	487.5	65	BLUE
S3	525	575	550	50	GREEN
S4	580	625	602.5	45	ORANGE
S5	630	690	660	60	RED
S6	705	745	725	40	RED EDGE
S7	750	820	785	70	NIR 1
S8	825	950	887.5	125	NIR 2
S9	-	-	-	-	RGB

Distinct bands of the MAIA MV sensor, from Sal Engineering©

APPENDIX B

APPENDIX B

MATRICE 600 PRO SPECIFICATIONS

AIRCRAFT

Diagonal Wheelbase	1133 mm
Dimensions	1668 mm × 1518 mm × 727 mm with propellers, frame arms and GPS mount unfolded (including landing gear) 437 mm × 402 mm × 553 mm with propellers, frame arms and GPS mount folded (excluding landing gear)
Package Dimensions	525 mm × 480 mm × 640 mm
Weight (with six TB47S batteries)	9.5 kg
Weight (with six TB48S batteries)	10 kg
Max Takeoff Weight Recommended	15.5 kg
Hovering Accuracy (P-GPS)	Vertical: ±0.5 m, Horizontal: ±1.5 m
Max Angular Velocity	Pitch: 300°/s, Yaw: 150°/s
Max Pitch Angle	25°
Max Wind Resistance	8 m/s
Max Ascent Speed	5 m/s
Max Descent Speed	3 m/s
Max Service Ceiling Above Sea Level	• 2170R propellers: 2500 m ; • 2195 propellers: 4500 m
Max Speed	40 mph / 65 kph (no wind)
Hovering Time* (with six TB47S batteries)	No payload: 32 min, 6 kg payload: 16 min
Hovering Time* (with six TB48S batteries)	No payload: 38 min, 5.5 kg payload: 18 min
Supported DJI Gimbals	Ronin-MX; Zenmuse Z30, Zenmuse X5/X5R, Zenmuse X3, Zenmuse XT; Zenmuse Z15 Series HD Gimbal: Z15-A7, Z15-BMPCC, Z15-5D III, Z15-GH4
Flight Control System	A3 Pro
Propulsion System	• Motor model: DJI 6010 • Propeller model: DJI 2170R
Retractable Landing Gear	Standard
Operating Temperature	14° Fto 104° F (-10° C to 40° C)

APPENDIX C

APPENDIX C

LIST OF REFELECTANCE ABBREVIATIONS

Predictor					Abbreviation
Single band	Purple				Purple
Single band	Blue				Blue
Single band	Green				Green
Single band	Orange				Orange
Single band	Red				Red
Single band	Red Edge				Red Edge
Single band	Near IR				NIR
Ratio	Blue		Purple		B:P
Ratio	Green		Purple		G:P
Ratio	Orange		Purple		O:P
Ratio	Red		Purple		R:P
Ratio	Red Edge		Purple		RE:P
Average	Ratios		Purple		Avg(P ratios)
Ratio	Purple		Red Edge		P:RE
Ratio	Blue		Red Edge		B:RE
Ratio	Green		Red Edge		G:RE
Ratio	Orange		Red Edge		O:RE
Ratio	Red		Red Edge		R:RE
Average	Ratios		Red Edge		Avg(RE ratios)
Inverse band	Green				1/G
Inverse ratio	Blue		Purple		1/B:P
Inverse ratio	Blue		Red Edge		1/B:RE
Inverse ratio	Red		Red Edge		1/R:RE
Inverse Average	Ratios		Purple		1/Avg(P ratios)
Inverse Average	Ratios		Red Edge		1/Avg(RE ratios)
NDVI (Ratio)	Near IR	- Red	/ Near IR	+ Red	NDVI
Ratio	Near IR	- Red Edge	/ Near IR	+ Red Edge	NIR-RE/NIR+RE
Ratio	Purple	- Blue	/ Purple	+ Blue	P-B/P+B
Ratio	Purple	- Green	/ Purple	+ Green	P-G/P+G
Ratio	Purple	- Orange	/ Purple	+ Orange	P-O/P+O
Ratio	Purple	- Red	/ Purple	+ Red	P-R/P+R

Predictor					Abbreviation
Ratio	Purple	- Red Edge	/ Purple	+ Red Edge	P-RE/P+RE
Average	Ratios		**Above B G O R RE -/+ P Palues**		Avg(P-/P+)
Ratio	Red Edge	- Purple	/ Red Edge	+ Purple	RE-P/RE+P
Ratio	Red Edge	- Blue	/ Red Edge	+ Blue	RE-B/RE+B
Ratio	Red Edge	- Green	/ Red Edge	+ Green	RE-G/RE+G
Ratio	Red Edge	- Orange	/ Red Edge	+ Orange	RE-O/RE+O
Ratio	Red Edge	- Red	/ Red Edge	+ Red	RE-R/RE+R
Average	Ratios		**Above P B G O R -/+ RE Palues**		Avg(RE-/RE+)
Angle	Purple		Blue		Angle PB
Angle	Purple		Green		Angle PG
Angle	Purple		Orange		Angle PO
Sum	Angles		Purple		Sum(P angles)
Angle	Red Edge		Red		Angle RER
Angle	Red Edge		Orange		Angle REO
Angle	Red Edge		Green		Angle REG
Sum	Angles		Red Edge		Sum(RE angles)

BIOGRAPHICAL SKETCH

Ivy M. Hinson graduated from the University of Texas Rio Grande Valley in August 2019. She completed her Master of Science in Ocean, Coastal, and Environmental Science under Dr. Christopher A. Gabler and Dr. Abdullah F. Rahman. She previously completed her undergraduate degree at the University of North Carolina Wilmington in 2012 with a Bachelor's of Science in Biology. She may be contacted at ivyhinson@gmail.com.